Arabian Journal of Geosciences (2022) 15:1766
https://doi.org/10.1007/s12517-022-11057-7

ORIGINAL PAPER

Study of metasomatose iron deposit of Chaabet El Bellout (Ain Zana, NE of Algeria): mineralogy, geochemistry, and genetic model

Tarek Zerrouki[1,2] · Abdelhak Boutaleb[1] · Lounis Sami[1,3] · Ahmed Abderrahmane Semchaoui[1,2] · Abdallah Chabbi[4]

Received: 11 April 2022 / Accepted: 30 November 2022

Abstract

Chaabet El Bellout iron mine is located in the Medjerda Mountains, constituting a connection zone between the Maghrebides chain and the Saharan Atlas. This deposit is mainly embedded in Upper Cretaceous (Campanian and Maastrichtian) and Miocene limestones with clusters and veins replacing both carbonates and sandy-carbonate levels. In this study, field observations and mineralogical analyses combined with geochemical and oxygen isotopic data were used to determine the origin of the mineralizing fluid and the source of mineralization. The results indicate that the iron ore of Chaabet El Bellout is of medium quality resulting following two main phases: first, the replacement of Cretaceous carbonates by ankerite and siderite, followed by the alteration of iron oxides (hematite and magnetite), then, a deposit of high temperature sulfides, sulfosalts, and sulfates (pyrrhotite, pyrite, chalcopyrite, gray copper, and barite) in a fractured zone. However, the contribution of magmatic fluids cannot be excluded, as some samples reveal high V-Mo-Ni and Zn contents and a negative isotopic signature (-0.6‰ VSMOW) different from the rest of samples that all indicate positive values (0.6 to 1.6‰ VSMOW), suggesting the participation of metasomatic saline fluids interacting with marine carbonate levels deposited in the Cretaceous and Triassic formations.

Keywords Medjerda Mountains · Upper Cretaceous · Iron ore · Hematite · Oxygen isotope

Introduction

Several iron deposits are known in northeast of Algeria (Ouenza, Boukhadra, Khanga). These deposits are currently being explored and exploited by public mining companies. The Ain Zana region (NE of Souk Ahras city) is part of the metallogenic district located at the Algerian-Tunisian border; it is also attached to the Maghrebides chain nappe (Villa 1978). This region contains numerous siderite occurrences and metasomatic deposits of Ouenza, Boukhadra, and Jebel Jerissa (Pohl et al. 1986) hosted either in Triassic diapirs or in Cretaceous-Miocene formations (Kriviakine et al. 1989). These concentrations are epigenetic and occur as veins and clusters. In 1964, Rudis attributed the majority of these mineralizations to N-S and ENE-SWS faults.

The aim of this study is to determine the relation between various concentrations and their host rock, using textural, mineralogical, and geochemical studies on different rock and ore types, and isotopic oxygen data. Indeed, the Chaabet El Bellout mineralization has never been thoroughly studied to determine its origin. The deposit is located in the external domain of the Maghrebides chains, where the Triassic outcrops play a dominant role in the development of the thrust sheets. The iron ore lies within a Campanian carbonate facies. These new data classify this deposit in metasomatic type with a significant contribution of magmatic fluids that show traces that present a pattern detected by the geochemical data analysis illustrated in this article.

Communicated by Domenico M. Doronzo

✉ Tarek Zerrouki
zerrouki.tarek@gmail.com

[1] (LMMA) Faculty of Earth Sciences, University of Sciences and Technology Houari Boumedienne (USTHB), BP 32, 16111 Bab Ezzouar, Algiers, Algeria

[2] Faculty of Natural and Life Sciences and Earth Sciences, University of Djilali Bounâma Khemis Miliana, Ain Defla, Algeria

[3] Department Geology, Mouloud Mammeri University, UMMTO, Tizi Ouzou, Algeria

[4] Department of Agricultural Sciences, University of Mohamed-Cherif Messaadia University, Souk Ahras, Algeria

Published online: 09 December 2022

Geological setting

Chaabet El Bellout iron deposit is located at 630 km east of Algiers, 100 km southeast of Annaba city, 77 km southeast from Guelma, 30 km northeast of Souk Ahras city, and 50 km west from the Algerian-Tunisian border (Fig. 1). This mining concession is currently exploited by SOMIFER (Algerian Society of Iron Mines) with an exploitable ore reserve of 3.6 million tons (Kouzmine 1992). The extracted ore is sold to the El Hadjar (Annaba) iron and steel complex when the Fe_2O_3 content is high (> 45%), and to cement factories when the content is between 35 and 45%.

The Medjerda Mountains constitute the easternmost part of the external Tellian domain within the Algerian section of the Maghrebides (Fig. 2). The relative convergence of the Tethys between the North African and South European margins, since 18 Ma, created the Maghrebides and Atlas Mountains along North Africa. The latter extends over 2000 km from the Rif (Morocco) through Algeria and Tunisia to Sicily (Italy) (Abbassene 2017; Bouillin 1986; Chazot et al. 2017; Said 2011; Talbi et al. 2008). The Maghrebides are subdivided into three overlapping paleogeographic domains (Raoult and JF 1974), from north to south: the internal domain (Kabyle), the flysch domain, and the external domain (Tell).

The study area is part of the external alpine chain domain, corresponding to the Tellian zones (sillon). This area is characterized by marly to carbonate deposits originating from the Tellian sillon of secondary to Tertiary age (Bouedja 2010; Chabbi 2017; Vila 1980) and the series of countries that limit the alpine chain to the south (Chadi 1991; Vila 1980). The Triassic formations are the oldest in this area and are abnormally placed relative to the other litho-structural units (Chabbi 2017).

Triassic diapirs on the Algerian-Tunisian borders (Souk Ahras, El Ouenza, Mesloula, and Sakiet) outcrop due to tectonic movements and extend usually along NE-SW oriented anticlinal axes during the main uplift from the Upper Aptian to the Albian (Madre 1969; Martinez et al. 1991; Perthuisot et al. 1978). The dimensions of these structures vary from 0.2 × 0.5 km to 25 × 10 km (Garnit and Bouhlel 2017; Hlaiem 1999; Zouaghi et al. 2005).

Triassic outcrops occur as intrusive masses deformed by Neogene to Quaternary accidents in more recent sedimentary series Cretaceous or Tertiary (Perthuisot 1978; Perthuisot et al. 1999). The Triassic is composed of heterogeneous materials consisting of mixed clay fragments, gypsum, marls, greenish to reddish sandstones, limestone boulders with igneous rocks, black dolomites, and rare green rocks (Halimi 2008; Zanouda et al. 2019). Sedimentation continues in the Cretaceous with reef to peri-reef deposits (Mahjoubi and Samama 1983; Vila 1980). The Lower Cretaceous formations correspond to Barremian to Vraconian deposits that generally cover the anticlinal flanks along diapir axes composed of marno-carbonates (organogenic reef limestone, dolomite, marly limestone, etc.) (Dubourdieu 1957; Kraiem et al. 2015). As for the Upper Cretaceous, which outcrops in the region, it consists of formations dating from

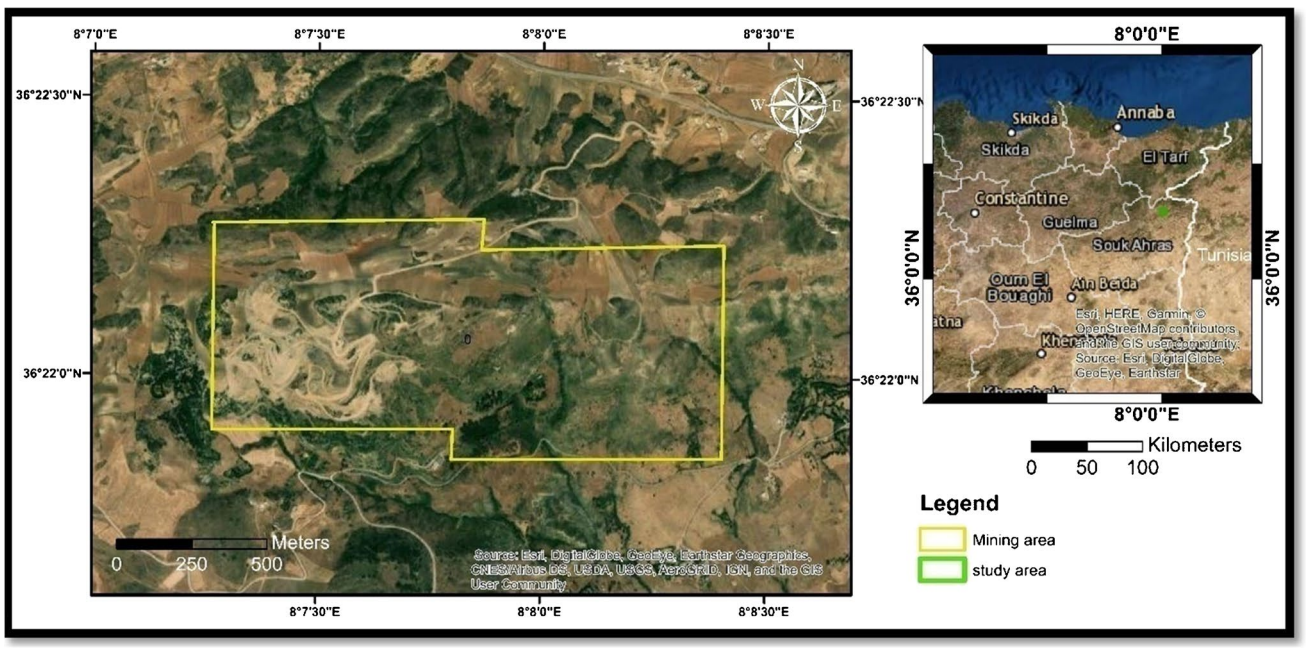

Fig. 1 Geographical position of the structure of Chaabet El Bellout

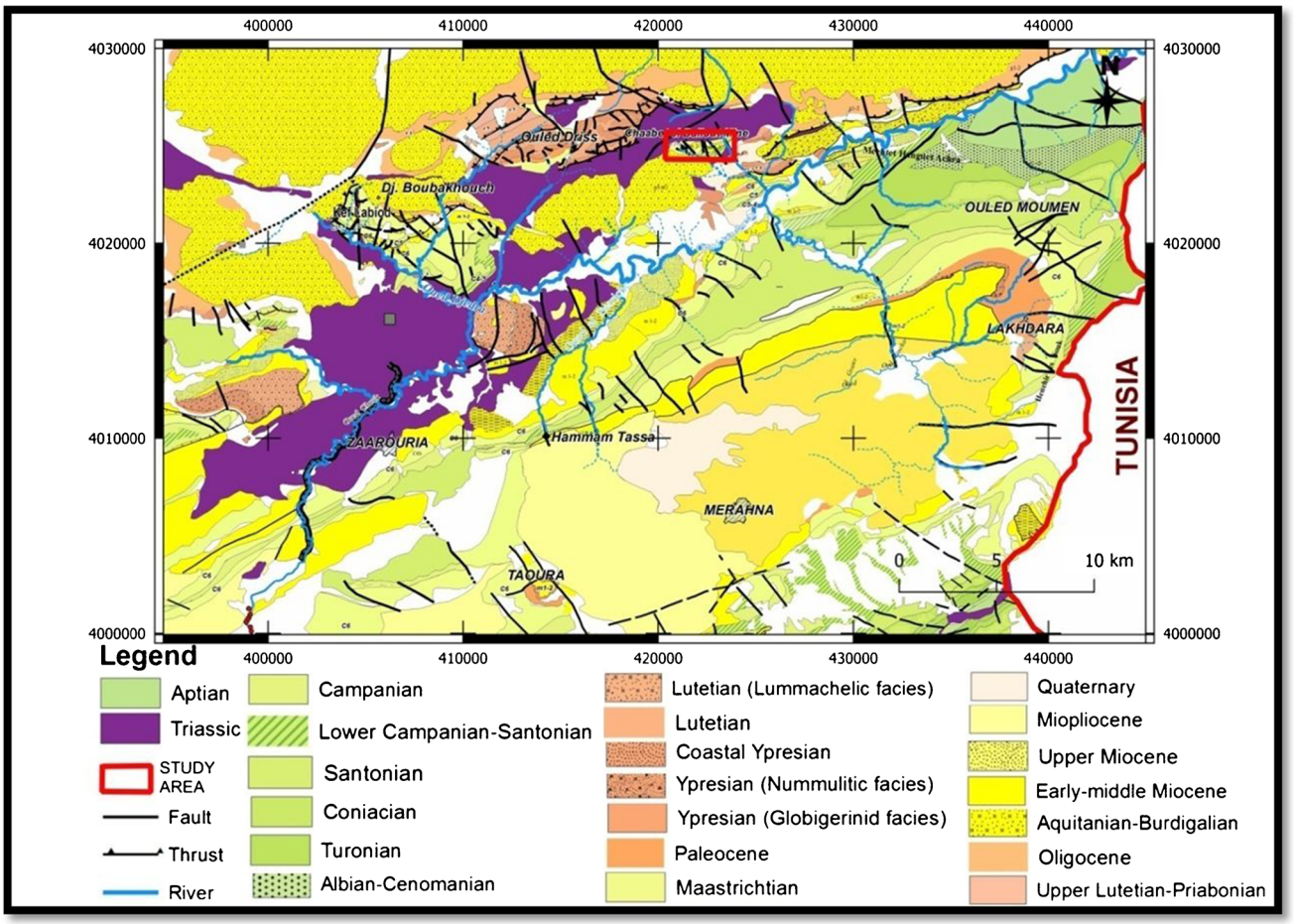

Fig. 2 Geological map of Medjerda mounts (Chabbi 2017)

the Cenomanian to the Maestrichtian. These thick series include marls, limestones, organic-rich limestones with clayey passages and two large limestone bars separated by marl-limestone alternations: the Lower Campanian and Upper Maastrichtian bars (Marzougui et al. 2015).

The Eocene layers are visible in this part of the Algerian-Tunisian border. The transition between the Maastrichtian and the Paleogene is marked by yellow marls followed by a phosphatic limestone deposit with flint nodules, Globigerine and Nummulite limestone (Ypresian to Lower Lutetian) and black marls (Bejaoui et al. 2011; Ferhi et al. 2018; Garnit and Bouhlel 2017). The Oligocene is represented by thick alternating clay and sandstone sequences often discordant with the older and darker strata (Ferhi et al. 2018). The Mio-Plio-Quaternary fill is composed of conglomerates, silty to sandy clays and sandy clays (Ferhi et al. 2018; Kraiem et al. 2015). This basin extends over several kilometers in a NE-SW orientation.

The compressional movement associated with the African and European plate convergence changes direction from NW–SE in the west to N-S in the east (Argus et al. 1989; Caire 1957; Gràcia et al. 2003; Said 2011).

The NE-SW oriented anticline (Dj. Graout) and syncline (Merahna, Lakhdara) (Chabbi 2017) are the main megastructures of the Algerian-Tunisian borders within the Medjerda Mountains originating mainly from the Upper Eocene "Atlas" compressive phase in Algeria and the Upper Miocene in Tunisia (Ferhi et al. 2018). In addition, major accidents shearing the Meso-Cenozoic cover formations resulted in large fractures that favored the upward migration of Triassic evaporates (Martinez et al. 1991). In addition, two major angular unconformities have been identified: the first between the Lower Miocene and the Paleocene and the second between the Mio-Pliocene and the Lower Miocene (Chabbi 2017).

The current structural aspect of the Medjerda Mountains is marked by thrust sheets and stacked allochthonous lithologic units on a para-autochthonous domain where the compressive phase between the Upper Eocene and the Lower Miocene occurs (Vila 1980). In addition, a polyphasic movement reaching a paroxysmal stress, oriented N-S developed a fracture network (N-S, E-W, and mainly NW–SE and NE-SW) that affects the entire ante-Miocene formations

(Chabbi 2017). This tectonic phase favored the structural stratification of lithological units with the same orientation as the Atlas Mountains (case of the Sallaoua unit) and led to small horizontal thrusts. The Eo-Cretaceous faults were then replayed in E-W and N-S directions during the Miocene and Mio-plio-quaternary compressive phase (Chabbi 2017; Martinez et al. 1991).

Chaabet El Bellout structure constitutes an allochthonous tectonic unit belonging to the Sellaoua domain (Chabbi 2017; David 1956; Vila 1980). It is represented mainly by Senonian (Campanian and Maastrichtian) carbonate facies (Fig. 3) overlain unconformably by sandstone and black marl of Miocene age in its central part. The entire unit is discordant with the Triassic band known as the Djelmana band common in the region (Fig. 4).

The Triassic complex is characterized by heterogeneous and versicolored (yellow, red, purple, etc.) clay levels (Fig. 5) and heterogeneous rock fragments containing metric blocks of saccharoid gypsum (David 1956). At Chaabet El Bellout, this complex occurs mainly in the northern part of the deposit and borders the Cretaceous and Miocene formations in an E-W direction.

The allochthonous series of Sellaoua of Cretaceous age are subdivided into two lithostratigraphic units about 100 m thick. The basal Campanian unit consists of alternating marls and yellow-gray limestones stratified in a highly fractured and often mineralized layer containing a pelagic fauna rich in Globotracana and Globingerina (Fig. 6a). The upper part is covered by the Maastrichtian unit which consists of metric layers of beige and relatively hard limestone, oriented N030° to N045° and dipping at 20° SE (Fig. 6b). In these limestones, microfauna is widespread with mainly Globigerines and Radiolarites, indicating deep marine sedimentation (Chabbi 2017).

The Miocene covers the central part of the deposit. This transgressive detrital formation is composed of a conglomeratic level at the base, covered by alternating black marl and marly sandstone over a 200-m thickness (Fig. 6c-d). According to David (1956), the structure of Chaabet El Bellout is an inverted syncline covered by Miocene formations at the center, while Campanian limestones and Maastrichtian limestones and marls outline its northern and southern flanks. In 1964, Rudis divided the Chaabet El Bellout into two distinct structural zones: a Cretaceous over Tertiary thrust zone in the western part and a synclinal zone deformed by multiple faults that developed into a horst structure, in the central and eastern part of the deposit. Furthermore, Chabbi (2017) suggests that, in the western part of Chaabet El Bellout, the existing structure results from the superposition of the Upper Cretaceous formations on the Miocene deposits. Indeed, the diapiric uplift of the Triassic material after the Lower Miocene deposition is closely associated with the folding, subsequent erosion, and structuring of the syncline.

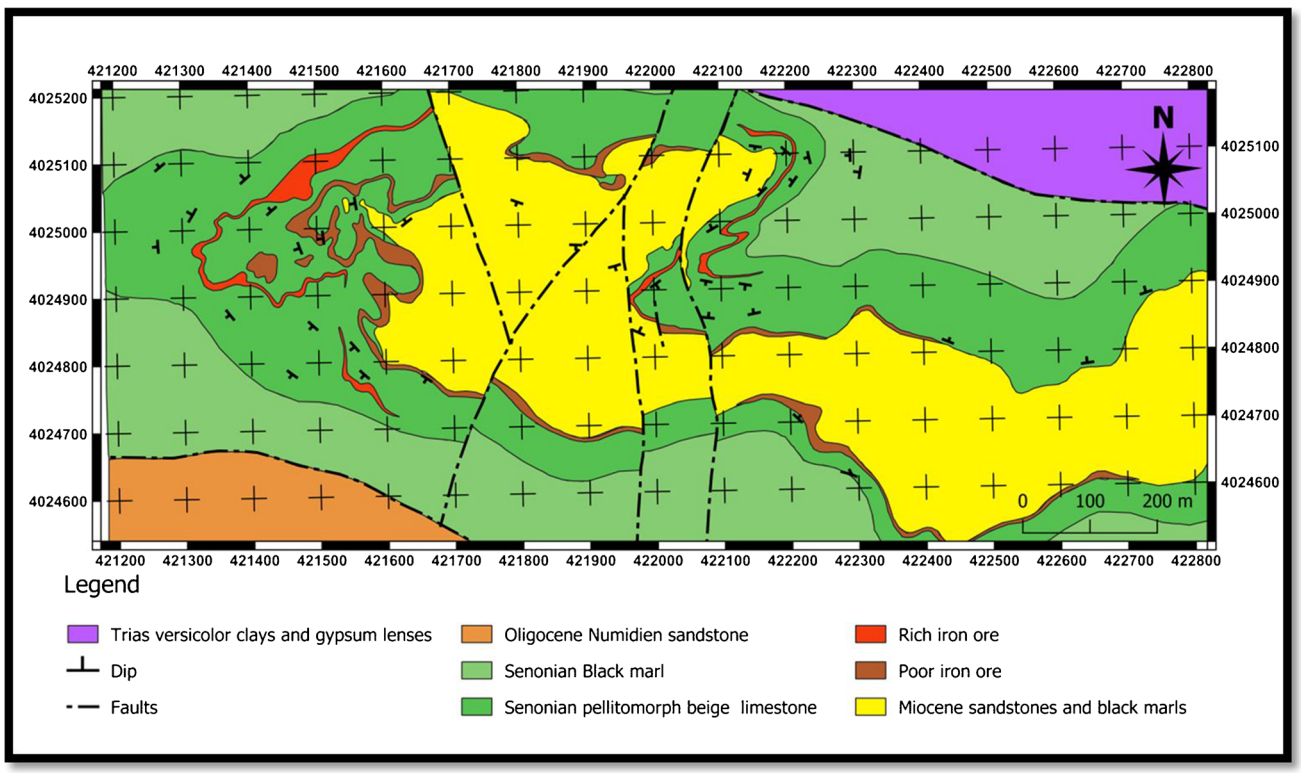

Fig. 3 Geological map of the Chaabet El Bellout mine (Kouzmine 1992)

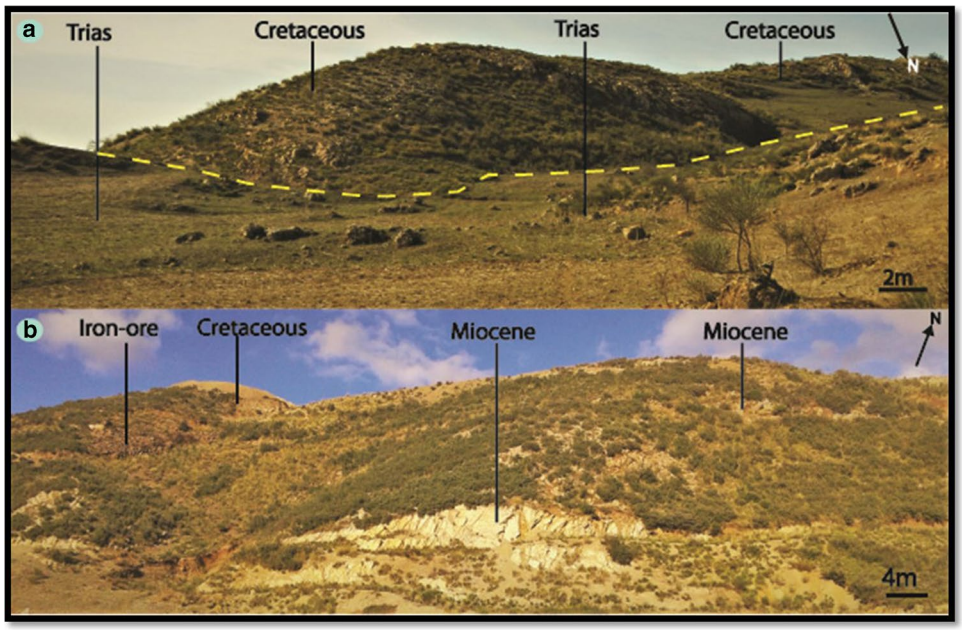

Fig. 4 Panoramic pictures showing all the geological formations of the Chaabet El Bellout structure. (**a**) Picture taken in the north east of study area. (**b**) Picture taken in the south of study area

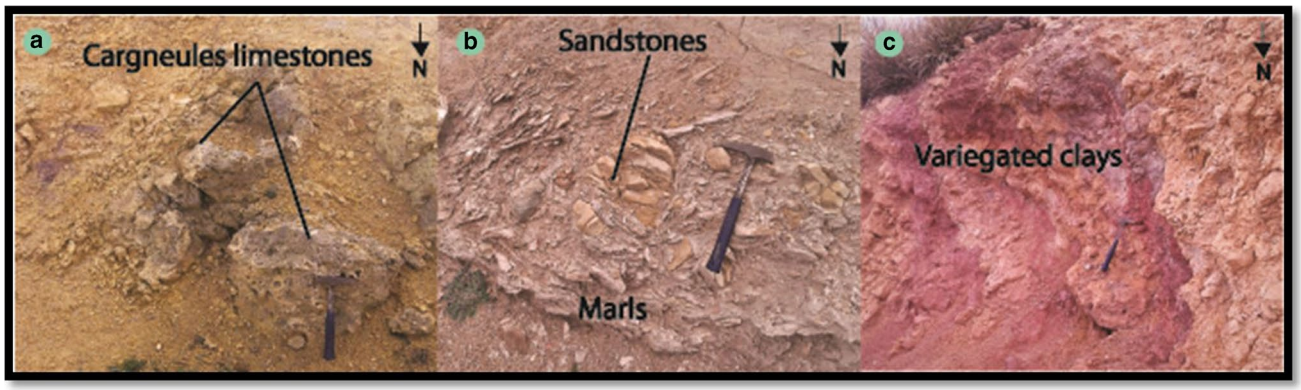

Fig. 5 Lithological facies of Trias at Chaabet El Bellout

Strike-slip faults filled with iron ore and calcite are easily identified in the field, as seen in the western part of the area with a N-S trending hematite-filled metric thickness in Campanian limestone. Similarly, N-S dextral strike-slip faults cutting through the Cretaceous and even the Miocene are observed in the eastern part of the deposit.

The iron ore deposit is located in the western flank of the Chaabet El Bellout syncline. The mineralization occurs in two forms: lenticular (ore clusters) and filling open spaces (veins).

The lenticular clusters are metric and located in two stratigraphic levels. The first level consists of white to beige limestones of the Upper Cretaceous (Rudis 1964). This mineralized level is Fe-rich with contents above 35%. These clusters represent the main and most profitable mineralization of this deposit. They are exploited due to their significant thickness, varying from 20 cm to 1 m. The second mineralized level corresponds to a carbonate rock contact between the Cretaceous and Miocene detrital facies consisting of an iron-poor sandstone with concentrations below 35%. This level results from the ferruginization of cemented carbonate sandstones (Fig. 7a).

The veins are not particularly economical as their thickness rarely exceeds 0.5 m (Fig. 7b). They are oriented mainly from N060° to N090° with a relatively steep dip to the north. Their extension is plurimetric but their depth is limited. They follow the fracture planes affecting the Cretaceous (Campanian) limestones and carbonate marls. Their distribution is particularly important in the central part of the deposit. This mineralization is then affected by later tectonics which results in E-W oriented reverse faults.

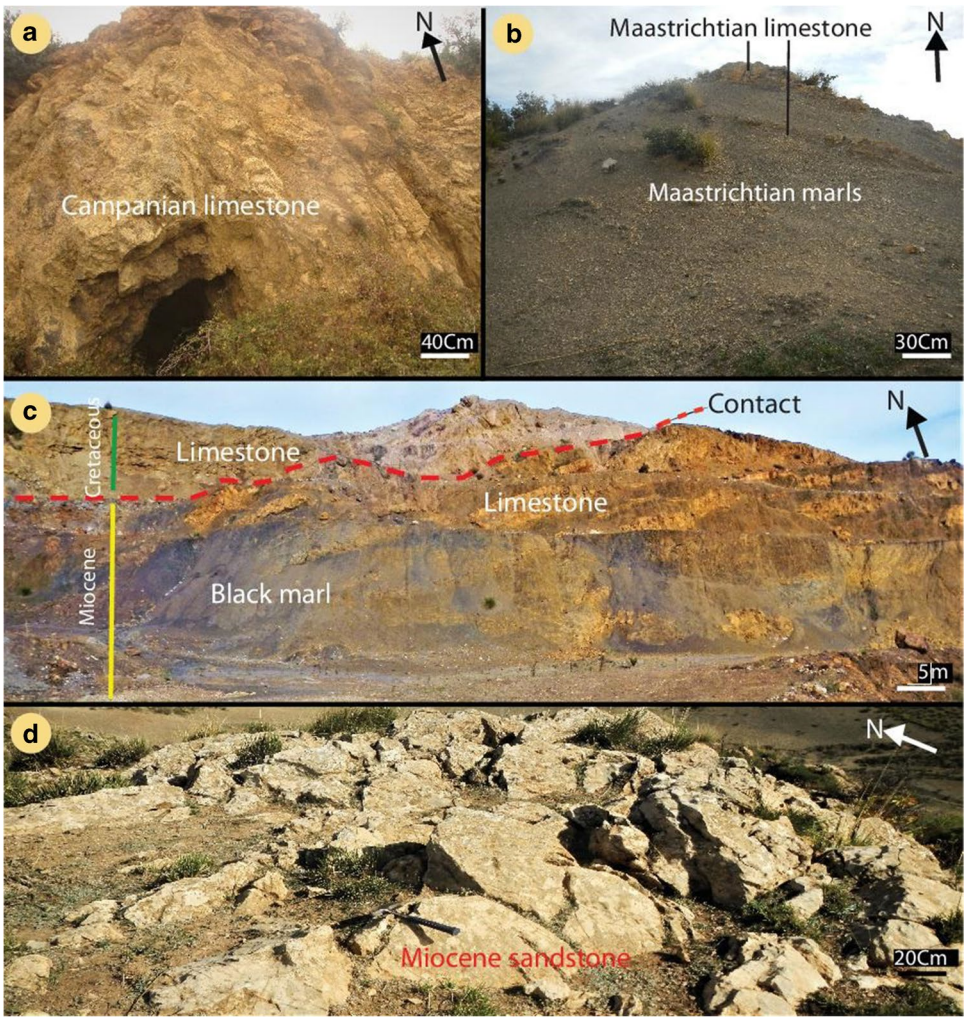

Fig. 6 Different facies outcrop at Chaabet El Bellout. (**a**) Exploration gallery in a folded Campanian limestone. (**b**) Carbonate marl formation of the Maastrichtian. (**c**) Photograph illustrating the series inversion in the western part of the Chaabet El Bellout Fe-Mine. (**d**) Miocene's sandstone

Material and methodology

Several field missions were conducted to understand the relationship between the geological parameters of the study area and the morphology, quality, color, and texture of the ore. From these observations, a relationship and dispersion of ore quality was established. A total of 50 samples were collected from different ore bodies and host rocks throughout the deposit.

These samples were the subject of a descriptive mineralogical study, by carving about thirty polished sections for the ore and twenty thin sections for the surrounding rocks, to examine with a Carl Zies Axiolab Pol double function optical microscope (natural light and reflected light). In addition, to identify and validate the mineral content, XRD was used at the CETIM Algeria laboratory.

Numerous samples were examined with a microscope and then scanned with the Tescan electron microscope in the Ceramines Agency laboratory (Dar El Beida Algeria). A total of 13 samples were analyzed by ICP-AES, including 6 host rock samples and 7 different iron ore samples. The geochemical analyses were performed at the ALS laboratory (Laboratory Group—SL Seville, Spain).

The Inductively Coupled Plasma Atomic Emission Spectroscopy (ICP AES) method consists of preparing 0.1 g of sample added to a lithium metaborate/lithium tetraborate stream, well mixed and melted in an oven at 1000 °C. The resulting melt is then cooled and dissolved in 100 ml of 4% nitric acid and 2% hydrochloric acid. The solution is analyzed by ICP-AES and the results are corrected for spectral interferences between elements. The oxide concentration is derived from the determined element concentration. If necessary, the total oxide content is determined from the concentrations of the ICP analysis and Losses on Ignition (L.O.I). A prepared sample (1.0 g) is placed in an oven at 1000 °C for one hour, cooled and then weighed and the percentage of L.O.I. is calculated from the weight difference.

Inductively Coupled Plasma-Mass Spectroscopy (ICP-MS) (Minor Element Analysis) for each sample prepared

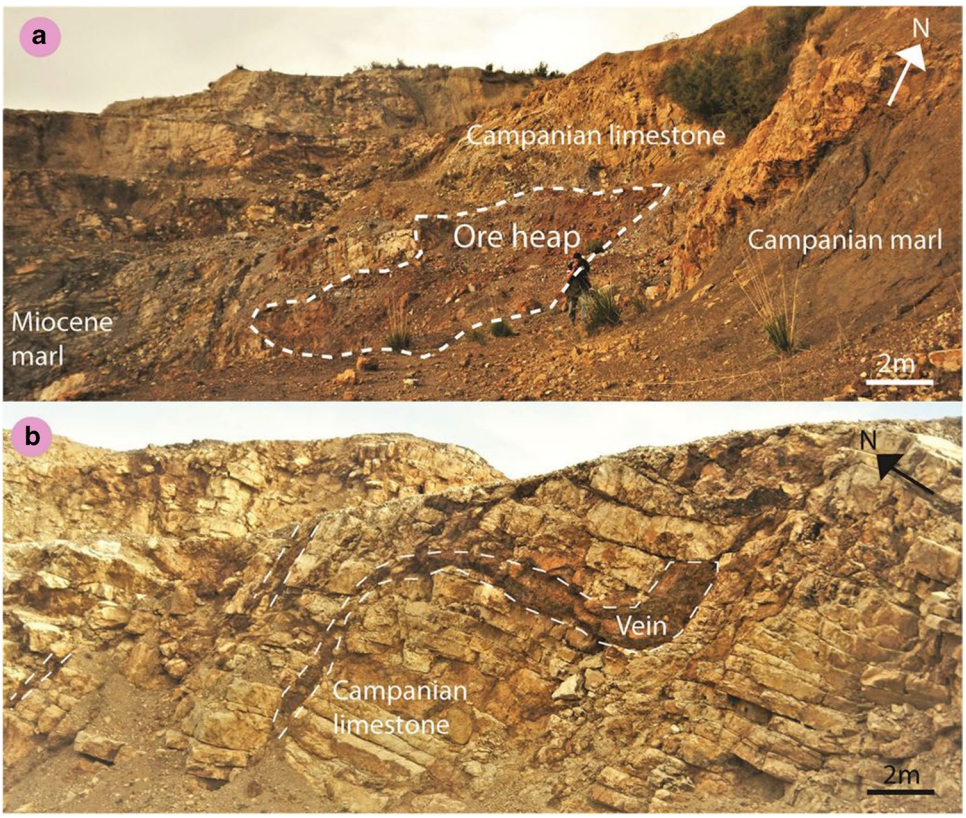

Fig. 7 Morphology of the ore-body at Chaabet El Bellout. (**a**) Iron cluster (heap) hosted in the carbonates of the Campanian along a fractured zone. (**b**) Iron vein hosted in beige Campanian limestones, folded and fractured after their deposition

by lithium borate ($LiBO_2/Li_2B_4O_7$) melt weighing 0.100 g is added to the lithium metaborate/lithium tetraborate stream, mixed well and melted in a furnace at 1025 °C. The resulting melt is then cooled and dissolved in an acid mixture containing nitric, hydrochloric, and hydrofluoric acids. This solution is then analyzed by inductively coupled plasma mass spectrometry.

Decomposition of samples by aqua regia (GEO-AR01) or 4-acid (GEO 4ACID) is a finishing method for base metals. Base metals and additional elements more appropriately analyzed by acid digestion can be reported with ME-MS81 either by aqua regia (ME-AQ81) or 4-acid digestion (ME-4ACD81).

Four oxygen isotope analysis of iron samples was performed at Miller Hall Department of Geological Sciences, Queen's University Kingston, Ontario, Canada. The O_2 was extracted from approximately 5 mg of sample, heated to 550–600 °C using the classical BrF5 procedure of Clayton and Epstein (1961), and analyzed by double entry on a thermo-Finnigan Delta PlusXP isotope ratio mass spectrometer (IRMS). The $\delta\ ^{18}O$ values are reported in delta notation (δ) in permille units (‰) relative to the international standard Vienna Standard Mean Ocean Water (VSMOW), with an accuracy of 0.4‰.

Results

Mineralogy

The main paragenesis of the Chaabet El Bellout mineralization, in all its forms, is relatively simple. It is marked by hematite as the main mineral in reddish to blackish clusters (Fig. 8a). Its texture is massive, veined, or boxed. When it is massive, it occurs in large millimetric to centimetric plates and in rare automorphic crystals. Iron carbonates represented by ankerite and siderite are generally found at depth (Halimi 2008; Kouzmine 1992). Brown siderite is present in residual deposits in the upper oxidized portion and transformed to hematite (Fig. 8b). Goethite is often associated with trace amounts of hematite and has a collomorphic character. The latter occurs as masses but rarely as druses or as well-crystallized orthorhombic crystals (Fig. 8c-e). The pyrrhotite-pyrite-chalcopyrite association represents the signs of a high temperature paragenesis that crosses the iron mineralization and occurs along the N-S fault in the center of the deposit.

Pyrrhotite occurs as very small, microscopic, automorphic grains identified by the hexagonal shape of their basal sections under the metallographic microscope Chalcopyrite

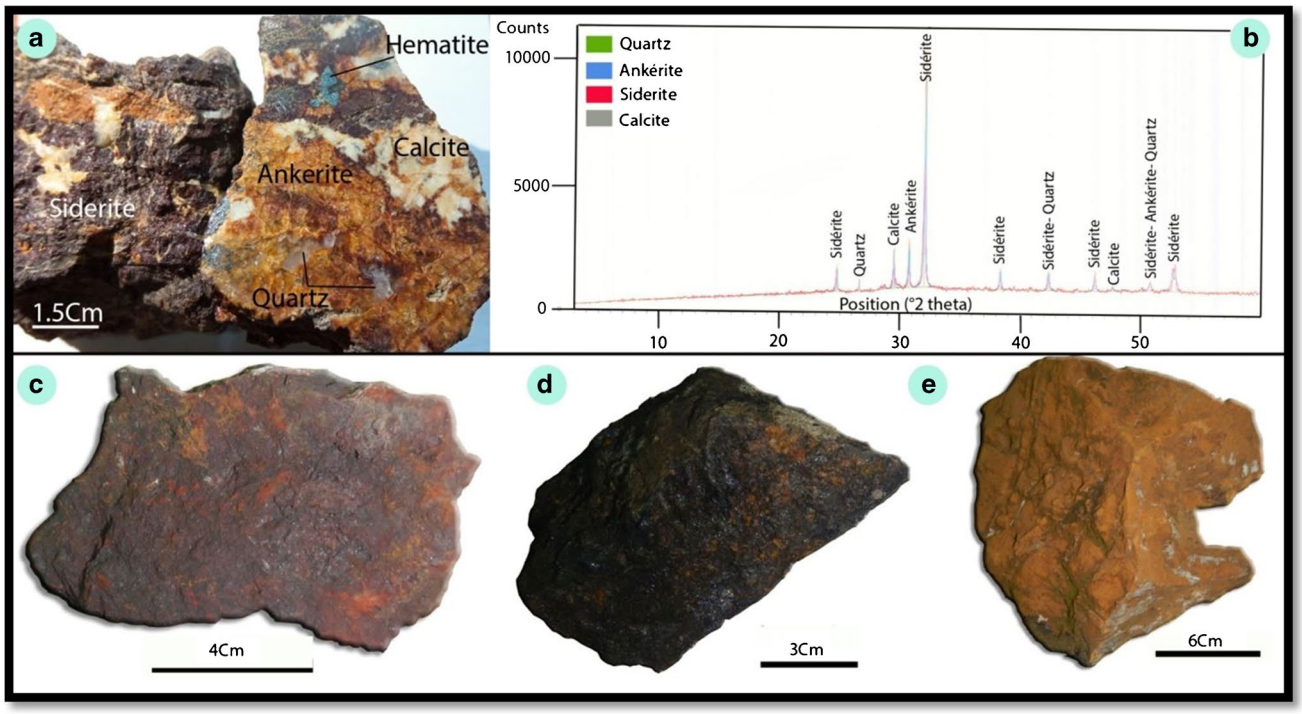

Fig. 8 Hand specimen photographs of iron ores in Chaabet El Bellout mine. (**a**) Carbonated iron ore and oxide (ankerite-siderite–hematite). (**b**) X-ray spectra of carbonated and iron oxide ore. (**c**, **d**) Massive hematite. (**e**) Limonite samples

occurs only with pyrrhotite. This mineral measures about 25 µm and is often surrounded by copper alteration minerals such as malachite, azurite, and covellite. Pyrite occurs as small automorphic cubes of millimeter size.

Barite is difficult to identify with the naked eye. It is composed of fine white flakes, millimetric to centimetric, which fills the cracks of the iron ore. It is often masked by the green color of malachite, which contrasts with the dark color of iron. In addition, barite is often associated with copper minerals and is found in fracture zones. Gray copper is the most common metallic mineral in this paragenesis, which is generally represented by the antimony pole (tetrahedral). It forms isolated replacement patches of a few centimeters, disseminated in the iron mass associated with barite. It is also found in highly fractured and altered pseudo-spherical millimetric grains in malachite and azurite. This mineral is often present in the eastern part of the mine. Calcite occurs as massive to centimetric scalenohedral and rhombohedral crystals. Scanning electron microscope (SEM) analysis revealed that the gray copper is destabilized into Pb-Sb and Cu-Fe oxides presented respectively by delafossite ($CuFe_3O_2$) in small automorphic patches up to 100 µm and rosiaite ($PbSb_2O_6$) (Pb-As) oxide.

Several structures characterize this iron mineralization, the most important being breccias, consisting of centimetric fragments of iron ore, and dolomitized carbonates embedded in calcite cement as small geodes. A massive structure composed of hematite and limonite clusters is also encountered, especially at the contact of the Upper Cretaceous limestones. In addition, other types of alteration structures such as vacuolar and vein structures (especially for secondary copper minerals) are observed (Fig. 9).

Initially, a diagenetic phase marked by calcite precipitation occurred and the first fluids arrived favoring their transformation into ankerite and siderite. Then, a supergene hydrothermal episode triggered the destabilization of siderite and ankerite resulting in hematite through meteoric fluids from the surface. A second episode of higher temperature hydrothermal phase occurred with the deposition of sulfides such as pyrrhotite, pyrite, and chalcopyrite in small aggregates and the minor release of sulfates and sulfosalts (barite and gray copper); the deposition and remobilization of pre-existing mineral concentrations along fractures, notably sub-meridian. The last late supergene hydrothermal phase caused the destabilization of gray copper and chalcopyrite to produce Pb-Sb oxides and malachite, azurite, barite, and barite (Table 1).

Geochemistry

Host rocks

Six host rock samples were analyzed for major oxidized element, trace element, and rare earth element (REE) geochemistry (Table 2). These include two Campanian limestones

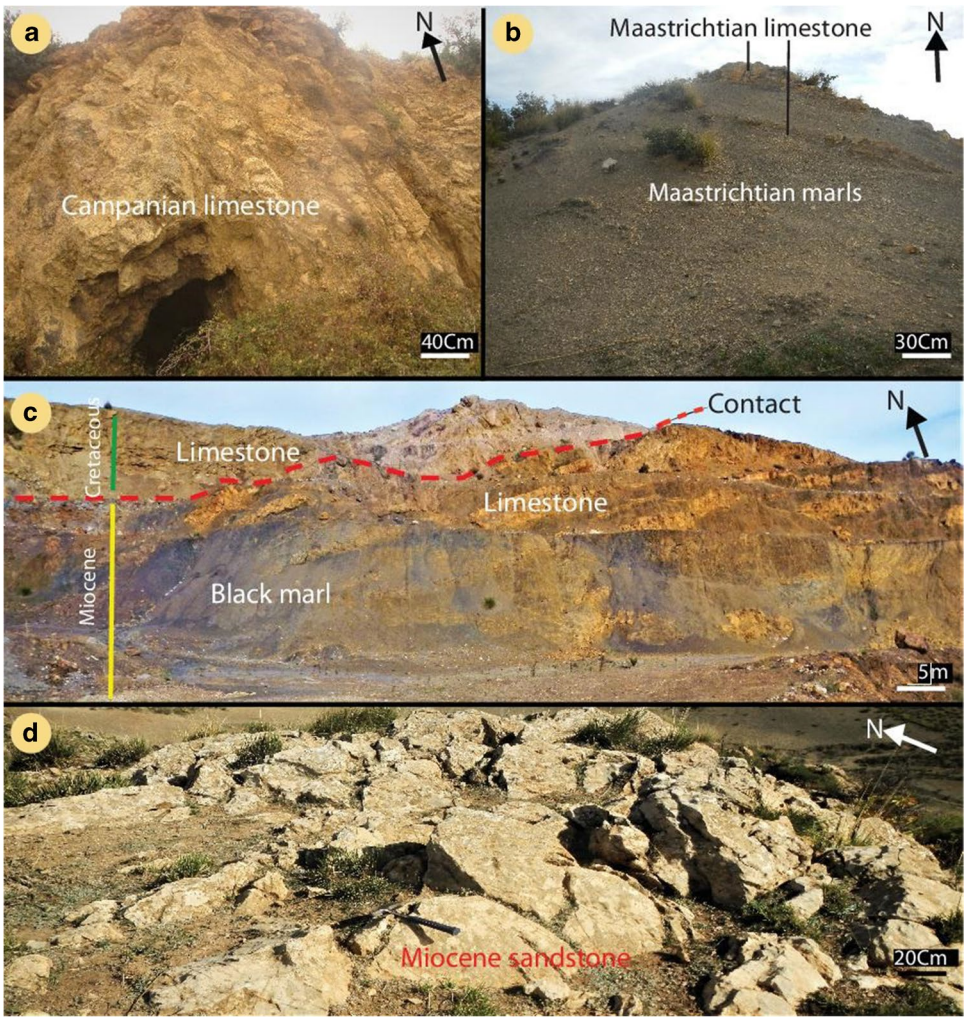

Fig. 9 Microphotographs of sulfide iron ores in Chaabet El Bellout mine. (**a**) Barite and altered sample of gray copper. (**b**) Microphoto-graphic of gray copper. (**c**) Microphotographic of sulfide (pyrrhotite-chalcopyrite and hematite). (**d**) SEM picture of copper and antimonies oxide (delafossite and rosiaite)

Table 1 Paragenetic sequence of ore, gangue and supergene minerals in the Chaabet El Bellout deposit

Mineral	Hydrothermal 1		Hydrothermal 2	Supergene
Calcite		FRACTURATION		
Ankerite				
Siderite				
Magnetite				
Hematite				
Goethite				
Limonite				
Pyrrhotite				
Pyrite				
Chalcopyrite				
Grey copper				
Barite				
Delafossite				
Rosiaite				
Malachite				
Azurite				

Table 2 Major (wt%). trace and rare earth element (ppm) contents of the Chaabet El Bellout rocks. CEB1: fine black marl; CEB11: white limestone pelitomorphic bench-stratified; CEB29: white limestone fossiliferous concoidal breack; CEB3: brown sandstone with carbonate cement, slightly altered; CEB9: fine black schitified clay; and CEB41: green amphibole sandstone

Sample ID	Cretaceous rocks			Miocene rocks		
	CEB 1	CEB11	CEB29	CEB 3	CEB9	CEB 41
Major elements (%)						
SiO_2	26,1	6,18	3,36	58,5	49,3	55
Al_2O_3	7,67	2,38	0,67	1,31	14,9	8,75
Fe_2O_3	1,89	1,39	1,04	0,76	5,58	20,2
CaO	33,9	50	52,5	21	9,44	2,64
MgO	0,41	0,18	0,57	0,14	1,45	1,07
Na_2O	0,04	0,02	0,01	0,03	0,2	0,05
K_2O	0,27	0,12	0,11	0,09	2,58	3,42
Cr_2O_3	0,015	0,004	< 0,002	0,47	0,018	0,11
TiO_2	0,43	0,11	0,04	0,08	0,75	0,21
MnO	0,05	0,07	0,06	0,02	0,04	0,11
P_2O_5	0,23	0,07	0,04	1,15	0,28	0,95
SrO	0,18	0,14	0,09	0,17	0,05	0,02
BaO	0,01	0,02	< 0,01	< 0,01	0,01	0,02
LOI	28,33	39,9	41,7	16,35	13,05	7,82
Total	99,5	100,58	100,19	99,65	97,65	100,37
Trace elements (ppm)						
Ba	67	164	15,6	31	115	143
Cr	100	30	10	340	130	800
Cs	6,06	1,96	0,55	0,51	51,1	22
Ga	10	3,6	1,8	2,6	20,1	20,1
Hf	1,6	0,5	0,2	1,9	5,1	3,2
Nb	7,5	1,9	1,2	5,1	17,8	6
Rb	16,1	5,4	3,4	3,6	128	175,5
Sn	8	< 1	< 1	< 1	2	2
Sr	1640	1250	755	1590	570	277
Ta	0,6	0,1	< 0,1	0,1	0,9	0,2
Th	4,1	1,16	0,45	1,99	10,1	9,04
U	9,13	1,23	4,27	9,86	3,14	4,22
V	104	37	17	17	108	185
W	3	1	1	2	2	2
Y	11,2	8,5	7,8	32,4	19,4	37
Zr	55	15	7	77	184	105
Ag	1,1	0,6	0,5	0.5	1,3	0,5
As	105	63	36	31	364	65
Cd	< 0,5	< 0,5	< 0,5	0.5	< 0,5	< 0,5
Co	11	4	2	4	11	14
Cu	183	14	57	40	20	13
Li	1390	370	40	170	230	180
Mo	3	< 1	1	1	3	1
Ni	32	13	7	6	44	31
Pb	62	9	24	20	34	11
Sc	8	3	1	3	12	22
TI	< 10	< 10	< 10	10	< 10	< 10
Zn	38	33	36	15	37	23
REE (ppm)						
Ce	30,8	11,2	5,4	36,9	73,9	126,5
Dy	1,95	1,17	0,94	4,81	4	8,27
Er	1,16	0,65	0,53	2,66	2,22	3,5

Table 2 (continued)

Sample ID	Cretaceous rocks			Miocene rocks		
	CEB 1	CEB11	CEB29	CEB 3	CEB9	CEB 41
Eu	0,71	0,35	0,38	1,4	1,12	2,93
Gd	2,51	1,31	1,08	5,79	4,43	12,05
Ho	0,39	0,21	0,19	0,91	0,75	1,39
La	17,1	6,8	4,7	18,4	35,7	44,3
Lu	0,17	0,09	0,07	0,3	0,32	0,35
Nd	15,5	6,1	4,2	22,6	31,9	60,8
Pr	3,74	1,49	0,93	5,12	8,19	14,6
Sm	2,71	1,44	1,04	5,43	6,02	14,1
Tb	0,33	0,18	0,17	0,82	0,65	1,58
Tm	0,16	0,08	0,06	0,31	0,33	0,41
Yb	1,07	0,57	0,47	2,27	2,18	2,57
Total REE	86.96	36.79	28.95	116.41	176.03	297.37
LREE	73.17	28.69	17.73	95.64	161.26	275.28

and a blackish shaly marl (CEB11, CEB29, and CEB1), a Miocene carbonate sandstone, black clay, and amphibole green sandstone (CEB3, CEB9, and CEB41).

The limestone rocks of Chaabet EL Bellout (CEB11 and CEB29) are marked by a CaO content ranging from 50% to 52.5% and LOL content ranging from 39.9 to 41.7% due to high calcite concentration. Major elements in these limestones range between 5.9% and 10.52% due to their non-CaO-Lol composition ($=SiO_2+Al_2O_3+Fe_2O_3+TiO_2+MnO+MgO+Na_2O+K_2O+P_2O_5$). The SiO_2 and Fe_2O_3 contents vary between 3.36% and 6.18% and 1.04% and 1.39%, respectively. Small fluctuations are recorded in the Al_2O_3 (0.67 to 2.38%), TiO_2 (0.4–0.11%), and MgO (0.18–0.58) contents. The results indicate a negative correlation between SiO_2 and CaO (correlation coefficient r =—0.58) suggesting that both elements do not originate from the same source. The silica originates from siliclastic sediments (Armstrong-Altrin et al. 2003) while CaO originates from carbonate cements associated with variation in carbonate contribution in high carbonate deposits (Bakkiaraj et al. 2010; Einsele et al. 1991).

MnO content is very moderate (0.06–0.07%) as is the alkaline element Na_2O+K_2O (0.12–0.14%). It is noted that the NaO_2 content is lower than 0.05%, which suggests a freshwater supply (El Hefnawi et al. 2010). The low MgO concentration (average 0.50%) and high CaO concentration indicate a low dolomitization rate (Temur et al. 2009). However, in the blackish shale marl, we recorded an average CaO content of 33.9%, LOL of 28.33%, a higher SiO_2 content of 26%, and an average Al_2O_3 content of 7.67%. For the remaining major elements Fe_2O_3-MgO-Na_2O-K_2O-P_2O_5-MnO-TiO_2, the values average or lower than are 1.89–0.41%, 0.31–0.43%, 0.23–0.05%, and 0.18–0.43%, respectively. The trace element contents of these carbonates are variable; we note a fairly high Sr content compared to average, especially for CEB1 and CEB11 (1640–1250 ppm) and a low to medium level for CEB29 (750 ppm). Ba content is high in CEB11 (165 ppm) and depleted in CEB1 and CEB29 (67–15.6 ppm).

The analyzed limestone and marl samples show low depletion of ferromagnesian trace elements such as Co, Cr, Ni, and V. High field strength elements (HFSE) such as Zr, Y, Nb, Hf, Th, and U are present in low concentrations in these carbonates. In addition, the total REE content in the carbonate rock samples is relatively moderate, ranging from 28.95 to 36.79 ppm, while it reaches 86.96 ppm in the marl samples.

In sandstone and clay samples from the Miocene, SiO_2 concentrations are low, ranging from 55 to 58.5% for sandstones (CEB 41 and CEB 3) and 49.3% for black clays (CEB9). Al_2O_3 contents are high in clays (14.9%) and low in green amphibole sandstones (8.75%) and sandstones (1.31%) compared to the CCU. The latter shows a CaO content of 21% suggesting that these sandstones are carbonate. Also, the green amphibole sandstones are more ferriferous with 20.2% of Fe_2O_3 content. In addition, the concentrations of MgO, Na_2O, K_2O, TiO_2, MnO, and P_2O_5 are generally low, varying, respectively, from 0.14 to 1.45%, 0.03 to 0.2%, 0.09 to 3.42%, 0.08 to 0.21%, 0.02 to 0.11%, and 0.28 to 1.15%.

K_2O content ranges from 2.58 to 3.42% in black clays and green amphibole sandstones, respectively. The overall low concentrations of Fe_2O_3 and TiO_2 in carbonate sandstones. However, black clays and amphibole sandstone record a higher content of those two major elements (Fe_2O_3 and TiO_2). The contents of Large-Ion Lithophile Elements (LILE) such as Ba, Sr, Rb, Ba, and Th in sandstones and black clays range from 31 to 143 ppm, 277 to 1590 ppm, 3.6 to 175.5 ppm, and 1.99 to 10.1 ppm, respectively. This rock (green amphibole sandstone) presents several trace element anomalies (higher than average content for elements such as

Cr-Ba-Rb (800–143-175 ppm). The overall RRE content is also high compared to all other samples at 286.27 ppm, with a dominance of LRE at 275.28 ppm.

Iron ore

A geochemical analysis of the Chaabet El Bellout ore bodies was conducted to determine the distribution pattern of iron with associated trace elements. All geochemical data of major, trace, and REE elements are reported in Table 3. The elements, particularly Fe_2O_3, reach very high values ranging from 63.9% to 83.1%. Dark colored hematite (CEB24 and CEB40) is the most abundant mineral occurring as clusters in the Cretaceous facies. In contrast, the lowest concentration of iron ore with high SiO_2 content (18.44%) is recorded in sample CEB21 (hosted in a Miocene sandstone), but with low values of Al_2O_3, K_2O, CaO, MgO, TiO_2, and P_2O_5. However, two samples present high levels of Al_2O_3 (CEB21: 2.32% and CEB50: 4.53%) indicating a detrital contribution but their low TiO_2 content indicates a trivial contamination (Ndime et al. 2008). A significant CaO content is reported in CEB60 with 5.84%.

In an iron deposit, it is necessary to examine the distribution of Fe_2O_3 content relative to other major oxides (Fatiou et al. 2019). In this study, Fe_2O_3 presents negative correlations with SiO_2 ($r = -0.94$), Al_2O_3 ($r = -0.43$), MgO ($r = -0.56$), Na_2O ($r = -0.06$), K_2O ($r = -0.71$), TiO_2 ($r = -0.48$), and P_2O_5 ($r = -0.35$) and positive correlations with MnO ($r = 0.12$) and CaO ($r = 0.14$). This negative correlation between iron and silica and alumina is associated with hematite and goethite, while silica and alumina are reflected by the presence of quartz and a clay portion (Koteswara et al. 2011).

The Fe ore presents low content of metals such as (Cd, Co, Cr, Cu, Hf, Mo, Nb, Ni, Pb, Rb, Ta, Th, U, V, W, Zn, and Zr), except for sample CEB24 indicating significant and abnormal values of Cu (5340 ppm), Ag (90 ppm), and As (1060 ppm), respectively, and sample CEB50, which contains high concentrations of V (190 ppm), Mo (107 ppm), Ni (95 ppm), and Zn (174 ppm). On the other hand, sample CEB60 contains a higher concentration of Ba (898 ppm) and Sr (202 ppm) compared to other samples.

The correlation coefficients calculated between Fe and trace elements revealed a relatively good correlation between Fe and Cr, Nb, Th, U, V, Y, Mo, Sc, Sn, W, and Li, and a weak correlation between Fe and Ba, Co, Cu, Pb, Zn, Zr, Hf, Rb, Ta, and Tl. However, a negative correlation was observed with Ni.

The total REE content of the ore samples is relatively low ranging from 8.1 ppm (CEB24) to 59.2 ppm for sample CEB50 and the average REE content is about 25.65 ppm.

Data analysis indicates a significant enrichment of light rare earth elements compared to heavy rare earth elements with an average of 86% and a LREE/HREE ratio of 6.23. It should be noted that all Chaabet El Bellout Fe ore samples share similar PAAS normalized REE signatures (Pourmand et al. 2012), with a pronounced enrichment of light rare earth elements compared to heavy rare earth elements. This is confirmed by the La/Yb PAAS ratio, which varies between 0.1 and 0.81 (mean = 0.46). All samples show positive Eu PAAS anomalies ranging from 0.13 to 2.00 (average Eu/Eu* = 1.32) and Y PAAS ($Y/Y^* = 1.3$).

Stable isotope

Table 4 reports the oxygen stable isotope data performed on four (04) magnetite samples separated by different types of iron ore. The $\delta^{18}O‰$ isotope ratio values are negative (-0.6‰) for sample CEB50 and positive for the other three: CEB24 (0.4‰), CEB17 (1.3‰), and CEB40 (1.6‰) represent experimental calculation curves performed on oxygen isotope fractionation of iron oxides (hematite, magnetite, and mirmite) in equilibrium with hydrothermal fluids (Clayton and Epstein 1961; Cole et al. 2004). The $\delta^{18}O$ values of iron oxides vary during hydrothermal alteration because it involves mixing between oxygen from iron oxides and oxygen supplied by the fluid (Thorne et al. 2009). Oxygen isotope analysis on magnetite from the Mariela IOA deposit revealed a $\delta^{18}O$ value of 1.49 ± 0.04 ‰ and on the Mineville IOA a $\delta^{18}O$ value of -0.79 ± 0.03 ‰. The $\delta^{18}O$ values of the El Laco magnetite range from 4.00 ± 0.10 ‰ (LCO-39) to 4.34 ± 0.10 ‰ (LCO vein) while that of the Kiruna deposit is 1.76 ± 0.25 ‰ ($n = 2$) (Bilenker et al. 2016; Johnson et al. 2013; Nyström et al. 2008; Rhodes and Oreskes 1999). The moss-type magnetites from the Bafq district (Iran) have lower oxygen isotopic values ($\delta^{18}O$: -0.45 to 0.44‰) than the massive magnetite ($\delta^{18}O$: 2.87 to 5.27‰) (Mehdipour Ghazi et al. 2019). Thus, the $\delta^{18}O$ values of the three Chaabet El Bellout samples (CEB17, CEB24, and CEB40) are consistent with the data recorded in the Kiruna deposit. In sample CEB50, the $\delta^{18}O$ value is close to that of the Mineville deposit.

The $\delta^{18}O$ contents of the studied Chaabet El Bellout deposit are plotted in the diagram of Nyström et al. (2008) and compared with the oxygen isotopic contents obtained on magnetite in some studied deposits. The results of the $\delta^{18}O$ measurements in the Chaabet El Bellout magnetite samples are consistent with those found in the IOA magnetite deposits of the Chilean Iron Belt and IOA of the Kiruna district (i.e., Kiruna and Rängesberg). They are also in excellent agreement with moss-type magnetites from the Bafq deposit (Iran). All samples have a $\delta^{18}O$ value

Table 3 Major (wt%) trace and rare earth element (ppm) contents of the Chaabet El Bellout iron ore. CEB6: iron ore, hematitic-limonitized, CEB17: veinular iron medium rich, CEB21: iron ore medium rich silicified that crosses the sandstone levels of the Miocene, CEB24: black iron ore from NS fractures contains malachite muchetures, CEB40: black iron ore contains small barite beaches, CEB50: medium to rich iron red ore, and CEB60: red-brown iron ore from the east part of the deposit near the Trias Cretaceous limit

Sample ID	CEB 6	CEB 17	CEB 21	CEB24	CEB 40	CEB50	CEB 60
Major elements (%)							
SiO_2	4	5,24	18,45	4,44	3	8,58	2.66
Al_2O_3	0,62	1,02	2,32	0,2	0,84	4,53	0.79
Fe_2O_3	78,9	76,3	63,9	82,8	83,1	76,9	79.3
CaO	0,54	0,34	0,42	0,37	0,53	0,1	5.84
MgO	0,31	0,31	0,4	0,28	0,21	0,11	0.23
Na_2O	0,01	0,02	0,02	< 0,01	< 0,01	0,08	0.06
K_2O	0,06	0,19	0,42	< 0,01	0,07	0,49	0.07
Cr_2O_3	0,002	0,002	0,04	0,003	0,003	0,008	< 0,01
TiO_2	0,03	0,05	0,13	0,01	0,04	0,23	0.04
MnO	1,62	1,5	1,57	1,78	1,8	0,1	1.38
P_2O_5	0,01	0,03	0,2	0,01	0,01	0,55	0.05
SrO	0,01	0,01	0,01	0,01	0,01	< 0,01	0.01
BaO	0,04	0,02	0,05	0,01	0,1	0,03	0.1
LOI	14	13,55	12,15	10,4	9,98	7,47	11.3
Total	100,15	98,58	100,04	100,31	99,69	99,09	101.83
Trace elements (ppm)							
Ba	345	198	394	89,8	823	247	898
Cr	10	20	30	10	20	50	30
Cs	0,61	0,84	2,21	0,29	0,45	1,82	0.57
Ga	3,8	4,2	5,5	3,7	3,8	10,2	1.8
Hf	0,3	0,3	1,8	0,4	0,2	1,1	0.2
Nb	1	0,9	2,6	0,1	0,7	4,6	1
Rb	2,1	6,5	14,8	1,5	1,9	25,7	2.8
Sn	< 1	< 1	1	< 1	< 1	1	1
Sr	114	118	150	144,5	106,5	27,4	202
Ta	0,1	< 0,1	0,1	< 0,1	< 0,1	0,2	0.1
Th	1,64	0,55	1,83	0,15	0,43	5,89	0.44
U	1,62	2,22	2,03	1,45	0,79	9,42	1.42
V	17	42	35	5	29	190	20
W	13	1	2	2	1	33	< 1
Y	9,2	12,1	7,5	5,5	8,4	11,1	7.3
Zr	14	8	60	11	5	37	7
Ag	0,5	2,1	< 0,5	91,1	4	36,1	3.6
As	5	26	97	1060	264	885	104
Cd	< 0,5	< 0,5	0,6	1,7	0,7	< 0,5	< 0.5
Co	4	1	3	< 1	< 1	12	1
Cu	12	105	27	5340	549	158	24
Li	80	40	70	10	120	< 10	60
Mo	1	2	2	< 1	< 1	107	< 1
Ni	< 1	1	16	< 1	1	95	3
Pb	11	4	14	5	582	25	18
Sc	1	2	5	< 1	2	6	1
TI	< 10	< 10	< 10	< 10	< 10	< 10	< 10
Zn	32	8	17	169	32	174	130
REE (ppm)							
Ce	5,4	8,4	9,3	1,7	4	22,9	5.4
Dy	1,38	1,9	1,26	0,88	1,31	2,38	0.99
Er	0,68	1,11	0,85	0,74	0,93	1,19	0.68
Eu	0,66	0,53	0,42	0,09	0,3	0,52	0.39
Gd	1,74	1,91	1,45	0,5	1,16	2,35	1.07

Table 3 (continued)

Sample ID	CEB 6	CEB 17	CEB 21	CEB24	CEB 40	CEB50	CEB 60
Ho	0,24	0,39	0,26	0,21	0,28	0,44	0.26
La	3,9	5	5,1	1,1	2,4	11,8	4.4
Lu	0,08	0,12	0,14	0,12	0,11	0,16	0.08
Nd	4,2	5,4	4,7	1,1	2,4	10,8	3.7
Pr	0,9	1,14	1,14	0,24	0,56	2,78	0.79
Sm	1,42	1,7	1,26	0,37	0,88	2,25	0.92
Tb	0,26	0,32	0,21	0,12	0,19	0,39	0.19
Tm	0,07	0,16	0,14	0,12	0,11	0,17	0.1
Yb	0,59	0,83	0,81	0,81	0,78	1,07	0.45
Total REE	21.5	28.91	27.04	8.1	15.41	59.2	19.42
LREE	18.22	24.08	23.37	5.1	11.7	55.4	16.65
Eu/Eu *	2	1.42	1.47	0.13	1.36	1.07	1.77
Ce/Ce*	0.66	0.81	0.89	0.76	0.79	0.92	0.66

Table 4 Results of oxygen $\delta^{18}O$ isotope in magnetite

Samples	Description	$\Delta^{18}O‰$
CEB17	Iron from vein	1.3
CEB24	Black iron ore	0.4
CEB40	Black iron ore	1.6
CEB50	Iron red ore	-0.6

below 2‰ corresponding to the limit that differentiates orthomagmatic (igneous) magnetite from base-temperature hydrothermal magnetite (Taylor et al. 1967).

Discussion

Mineralogical implications

The morphology of mineralized clusters and veins hosted in Cretaceous to Miocene formations clearly indicates epigenetic mineralization. The primary mineral paragenesis is marked by siderite found in deep mineralized levels intersected by drill in 2017 and detected by XRD. Due to hydrothermal-metasomatic solutions, alteration of siderite to hematite occurred under different pH and temperature–pressure (Otake et al. 2007). The low siderite content of this metasomatic Fe ore is also considered to be of early diagenetic origin and supports the very high metasomatism as well. In addition, the presence of minor dolomite and ankerite is the result of siderite replacing primary diagenetic calcite (Klein and Beukes 1993). The massive metasomatic iron ore formed as a result of hematization of the primary siderite ore after a late arrival of saline or hydrothermal metasomatic fluids during diapiric ascent.

Geochemical implications

Host rocks

The negative correlation between SiO_2 and CaO on all samples (correlation coefficient r =—0.58) indicates that the two (2) elements are probably from different sources. Silica is from siliclas sediments (Armstrong-Altrin et al. 2003) while CaO is from carbonate cements, consistent with the variable contribution of carbonates in deposits with high carbonate content (Bakkiaraj et al. 2010; Einsele et al. 1991). The low concentration of MgO (average of 0.50%) and high concentration of CaO in the carbonates indicate low dolomitization rates (Temur et al. 2009).

The high silica content compared to other detrital oxides (alumina) in carbonate rocks is associated with the presence of either biogenic intra-basinal silica or pure quartz grains (Figari et al. 2015; Kennedy et al. 1998), confirming the low clay and authigenic mineral content in limestones (Temur et al. 2009).

It is noted that NaO_2 content is below 0.05% suggesting freshwater input (El Hefnawi et al. 2010) in all analyzed facies. K_2O content increases with the presence of feldspathic and micaceous minerals in Miocene detrital facies (CEB3, CEB9, and CEB41) (Ciccioli et al. 2020). High field strength elements (HFSE) such as Zr, Y, Nb, Hf, Th, and U are present in small concentrations in Cretaceous carbonates, indicating that these elements are known to be resistant to weathering (Bhatia and Crook 1986; Feng and Kerrich, 1990).

The depletion of REE in Cretaceous rocks is probably due to low clay fraction content in the studied limestones. Indeed, REEs are easily captured in clays (McLennan et al. 1989). However, the low concentrations may result from dilution of REE by carbonate minerals (Armstrong-Altrin et al. 2003). Er/Nd ratios (mol/mol) in Cretaceous limestone samples range from 0.10 to 0.12 and are close to the Er/Nd

ratio (0.27) of normal seawater (De Baar et al.1985) and higher than that of marl at 0.07. Furthermore, the (La/Yb) PAAS ratio of Cretaceous rocks varies between 0.75 and 1.13 (La/Yb) $s = 0.91$ and $n = 3$, which is close to the average value of carbonate sediments in the Arabian Sea (0.8 ± 0.2) (Nath et al. 1997). This suggests a shallow marine environment with low REE fractionation.

In addition, Eu values are important for understanding the physicochemical conditions of different carbonate depositional environments (Derry and Jacobsen 1990). The Eu/Eu * ratio of carbonate samples ranges from 1.22 to 1.73 (Fig. 10a) and indicates a positive Eu anomaly likely due to enrichment in detrital feldspar (Abedini and Calagari 2015; Armstrong-Altrin et al. 2003; Thomsen et al. 2008). This result is consistent with the significant Sr enrichment in these samples.

The overall low concentrations of Fe_2O_3 and TiO_2 in carbonate sandstones reflect the scarce titaniferous biotiotite, ilmenite, titanite, and magnetite (Armstrong-Altrin et al. 2003). However, black clays and amphibolic sandstones record a higher content of those two major elements (Fe_2O_3 and TiO_2), which indicates a ferromagnesian enrichment. This green amphibole sandstone presents several trace element anomalies (higher than average content for elements such as Cr-Ba-Rb (800–143-175 ppm) and REE content is also high compared to all other samples, which indicates a significant participation of the magmatic levels in the deposit process of this facies.

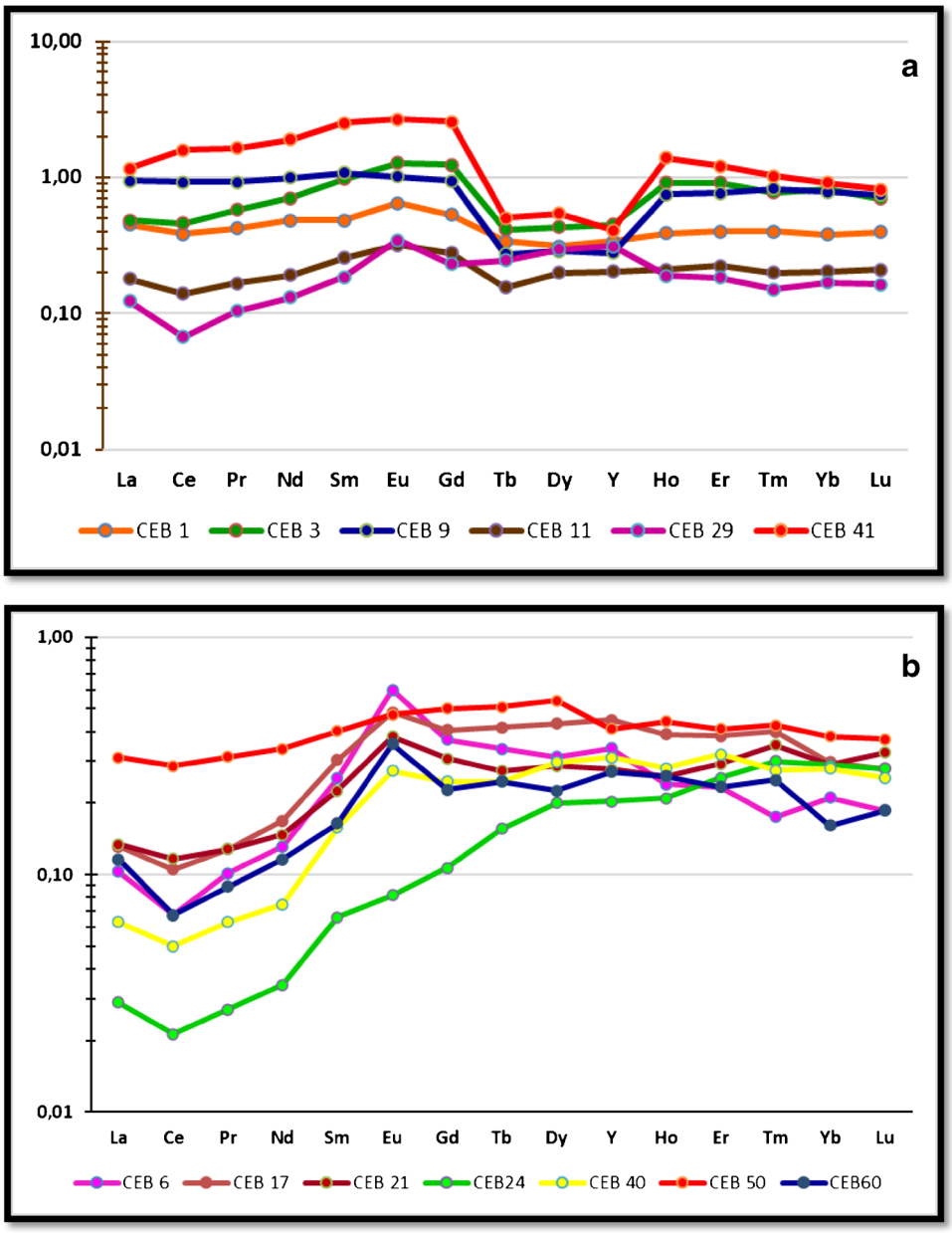

Fig. 10 PAAS normalized REE patterns of samples from Chaabet El Bellout Mine. (**a**) Host rock and (**b**) iron ore. PAAS values were taken from Taylor and Mclennan (1989)

The SiO_2/Al_2O_3, Na_2O/K_2O, and Fe_2O_3/K_2O ratios of the Miocene carbonate sandstone and amphibole sandstone are 6.28–44.65, 0.001–0.33, and 5.9–8.44, respectively. These values are consistent with the Fe-sand in the geochemical classification diagram of Herron (1988). In addition, the high Sr content reported in the clays and sandstones indicates that Sr may be directly related to calcite minerals (Baiyegunhi et al. 2017), which is consistent with the mineralogical study.

The Miocene rocks show TiO_2 and Zr values below 0.75% and 185 ppm, respectively, and indicate their igneous rock origin. This origin is further confirmed by the low TiO_2 $^{>}$0.75% and Ni $^{>}$44 ppm values. This is consistent with XRD data that indicate the presence of actinote and zeolite in the Miocene facies and suggest a magmatic contribution during the sedimentation process.

The AIC value reflects the ratio of original/primary minerals to secondary products such as clay minerals and provides information on the rock's alteration degrees. Indeed, during the alteration process, Ca, K, and Na elements are transported upwards and thus deplete the bedrock (Nesbitt et al.1997). The AIC is determined as follows:

$$\mathrm{ACI} = \left[\mathrm{Al_2O_3}/\left(\mathrm{Al_2O_3} + \mathrm{CaO^*} + \mathrm{Na_2O} + \mathrm{K_2O}\right)\right] * 100$$

where CaO * is the content of CaO incorporated in the silicate fraction. This value is calculated using the method of Mclennan (1993): CaO * (CaO * = CaO—$10/3 \times P_2O_5$).

Black clays and amphibole sandstones present very high AIC values (56.89 and 74.82%, respectively) indicating intense alteration. Facies with lower values include the less weathered Miocene carbonate sandstones and Cretaceous carbonate rocks (AIC less than 18.65%). The compositional variation index (CVI) is used to determine the alteration intensity, maturity, and predominant climatic conditions of the sediments related to the presence of clay minerals (Cox et al. 1995). The CVI is high for minerals with higher alteration rates and low for more stable minerals (less altered minerals) (Baiyegunhi et al. 2017). This index is derived as follows:

$$\mathrm{CVI} = (\mathrm{Fe_2O_3} + \mathrm{K_2O} + \mathrm{Na_2O} + \mathrm{CaO} + \mathrm{MgO} + \mathrm{MnO})/\mathrm{Al_2O_3}$$

If CVI > 1%, the sediment composition is immature and deposited in an active tectonic environment. However, when CVI < 1, the sediment composition is mature and deposited in a cratonic tectonic environment (Baiyegunhi et al. 2017). All Cretaceous and Miocene sedimentary rocks display CVI values greater than 1. Accordingly, the Miocene black clays and amphibole sandstones record the lowest values, ranging from 1.29 to 3.14, while the Cretaceous facies range from 4.76, to 81.02, indicating the least mature and tectonic environment of all these rocks. In addition, the K_2O/Na_2O ratio ranges from 3 to 68.4, suggesting that K-feldspar dominates plagioclase feldspar (albite) and that these sediments are very mature, which is consistent with CRI values (Wronkiewicz and Condie 1987).

Iron ore

The high iron content and depletion of silica and other major elements such as K_2O-Na_2O and REE indicate a relatively pure chemical precipitation of iron ore. The high CaO and low MgO values confirm the moderate presence of common carbonates such as calcite, dolomite, and ankerite in the massive ore (CEB6-CEB17 and CEB21).

The high Al_2O_3 content in some samples (CEB21 and CEB50) indicates a detrital contribution but their low TiO_2 content reveals trivial contamination (Ndime et al. 2008).

The negative correlation between iron and silica and alumina confirms the enrichment and ferruginization of the carbonate levels compared to a depletion of the latter in the detrital levels of Miocene age.

According to the mineralogical study, ferruginization is related to hematite and goethite, while silica and alumina are reflected in the presence of quartz and a clay portion (Koteswara et al. 2011).

The projection of these data in the Si versus Fe binary discrimination diagram indicates that ore samples lie at the boundary of hypogenic and hydrothermal ores, except sample CEB50 that falls in the field of volcanic origin mineralization. Iron ores can be classified according to their Fe_2O_3 content (Dobbins and Burnet 1982). The Chaabet El Bellout ore is considered poor according to the classification of with a total Fe content lower than 58%. However, according to Dill et al (2009), the average total iron content of a good Fe ore is between 30 and 65%.

The high Ba content in some samples (CEB6 and CEB21) is consistent with barite occurrence. Similarly, the relatively high Sr, Li, and Ba contents in host rock samples (CEB1 and CEB11) are associated with barite in some of the carbonate samples. The Cu, As, and Sb contents in some of the iron ore samples (notably CEB24) are explained by the presence of gray copper in an extremely fractured zone that was transformed into malachite, azurite, or oxide carbonates (delafossite, rosiaite) at a late stage.

The samples indicate a negative Ce anomaly. On the other hand, oxygenated marine waters display a strong negative Ce anomaly when normalized to PAAS, unlike anoxic waters. Thus, oxidation of Ce^{3+} significantly reduces Ce solubility and allows removal of Mn-Fe oxyhydroxides, clay particles, and organic matter.

It should be noted that in an oxidizing environment, $Ce3^{+}$ is transformed to $Ce4^{+}$ and removed from seawater (Yang et al.2015). The positive Ce anomaly in hematite ores is related to the reduction of Ce^{+4} to Ce^{+3} due to its low mobilization during the mineral formation.

High Sr concentrations in Cretaceous and Miocene facies from Chaabet El Bellout indicate deposition in an evaporated marine sedimentary basin where Sr enrichment is coupled with Ba depletion, which is rarely expressed mineralogically by barite. REE are good tracers of origin and deposition of iron concentrations (Bau and Dulski 1996; Bekker et al. 2010; Klein and Beukes 1993). Measurements of REE spectra indicate a positive Eu anomaly in iron ore samples, suggesting that lower temperature fluids are involved in the enrichment of iron and other elements (Michard et al.1993).

The Eu anomaly may indicate a volcanic origin. It can be caused by several processes, namely, possible seawater infiltration simultaneous to ore formation (Elderfield and Greaves 1982), oxidation at different scales (De Baar et al. 1988), or by diagenetic alteration (Fig. 10b).

Isotope implications

The results of oxygen isotope analyses performed on four magnetite samples indicate values ranging from 0.4 to 1.6 ‰. However, only one negative $\delta^{18}O$ value was recorded (-0.6‰ VSMOW) while the other three (03) are positive. This is explained by an inverse relationship between isotopic fractionation and temperature as isotopic fractionation is recorded when temperature decreases resulting in a depletion of heavy oxygen isotope $\delta^{18}O$ (Bouzenoune and Lécolle 1997). Furthermore, $\delta^{18}O$ values below 2‰ suggest late metasomatic alteration post-mineralization that affected the magnetite formed at the base by precipitation from a hydrothermal (Knipping et al. 2015) or by crystallization from a silicate melt (Bilenker et al. 2016; Childress et al. 2016; Knipping et al. 2015; Weis and Troll 2013). However, the positive $\delta^{18}O$ values (+0.6 to +1.3‰ VSMOW) may suggest the implication of isotopically altered seawater in hypersaline brines. This $\delta^{18}O$ enrichment is probably related to exchange reactions with deep marine carbonates of Triassic and Cretaceous age.

The pale orange box ($\delta^{18}O = 6.6–7.3$‰) represents magnetite in equilibrium with silicate magma with a $\delta^{18}O$ of 10‰. The vertical dashed line denotes the cutoff point between magnetite derived from silicate magma or magma-hydrothermal fluid, which in both cases would yield a $\delta^{18O} > 0.9$‰, and with low-temperature hydrothermal fluid with a $\delta^{18O} < 0.9$‰ (Johnson et al. 2008; Johnson et al. 2013).

The $\delta^{18}O$ contents of the studied Chaabet El Bellout deposit are plotted in the diagram of Nyström et al. (2008) and compared with oxygen isotopic contents obtained on magnetite in some deposits studied (Fig. 11). The results of $\delta^{18}O$ measurements in magnetite samples from Chaabet El Bellout are consistent with those found in IOA magnetite deposits from the Chilean Iron Belt and IOA from the Kiruna district (i.e., Kiruna and Rängesberg). They are also in excellent agreement with moss-type magnetites from the Bafq deposit (Iran). All samples display a $\delta^{18}O$ value below 2‰ corresponding to the limit that distinguishes orthomagmatic (igneous) magnetite from base-temperature hydrothermal magnetite (Taylor et al. 1967).

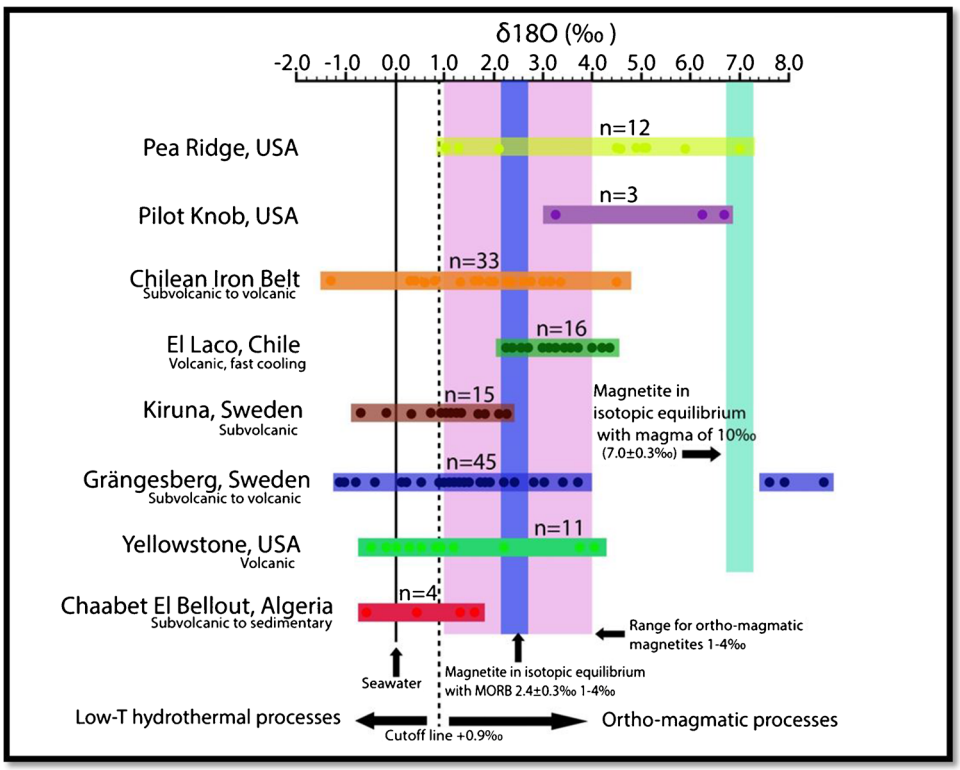

Fig. 11 Oxygen isotope ($\delta^{18}O$) values for magnetite from Chaabet El Bellout orebodies compared to those for other iron oxide deposits (adapted from Jonsson et al. 2013). Pink box ($\delta^{18}O = 1–4$‰) is range for orthomagmatic magnetite (Taylor 1967). Red box ($\delta.^{18}O = 2.2–2.6$‰) represents magnetite in equilibrium with mid-ocean ridge basalt (MORB)

Conclusion and genetic model

The iron-rich provinces on the Algerian-Tunisian border (Ouenza, Boukhadra, and Jebel Jerissa in Tunisia), including the Chaabet el Bellout mine, present a rather complex polyphase metallogenic chronology.

The process begins with a first phase marked by the replacement of Campanian limestones with iron carbonates (ankerite and siderite) at moderate temperatures (120–200 °C) according to the results obtained in the Ouenza iron deposit (Bouzenoune and Lécolle 1997). This phase includes a geochemical insertion of elements such as Fe and Mg and a reduction of Sr in the mineralized levels. The formation of siderite is controlled by the paleogeographic character of the Cretaceous series located in an emergent zone with a Triassic bedrock confining the environment and favoring the evolution of impure iron concentrations in the sedimentation process related to mineralizing fluids resulting from the expulsion of water from sedimentary basins (Madre 1969; Mahjoubi and Samama 1983; Thibieroz 1978); then, the contribution of hydrothermal fluids allowed the metasomatization of iron carbonates into hematite. Indeed, the oxygen isotope data of iron ore are less than 2‰ indicating a low-temperature saline source with an interaction of Triassic evaporite formations. In addition, the deposition of sulfides, sulfosalts, and sulfates is mainly associated with fractures and occurred after the deposition of hematite associated with another hydrothermal phase related to diapiric uplift during the Neogene. However, the contribution of volcanic rocks cannot be excluded given the presence of layers indicating the existence of volcanic syn-sedimentation contributions observed particularly in the Miocene layers (black zeolitic clays and green amphibole sandstones).

These results can be supported by the iron ore sample CEB50, indicating a hydrothermal-volcanic affinity and contents of metals with basic magmatic affinities such as V (190 ppm), Mo (107 ppm), Ni (95 ppm), and Zn (174 ppm). These recurring elements, which are poorly mobilized during the various hydrothermal alteration processes, suggest a volcanic contribution to the development of this mineralization (Beach et al. 1978; Winchester et al. 1977).

Declarations

Conflict of interest The authors declare no competing interests.

References

Abbassene F (2017) Contraintes chronologiques et pétro-géochimiques du magmatisme sur l 'évolution pré-et post-collisionnelle de la marge algérienne : secteur de la Petite Kabylie. Dissertation, University of Bretagne Loire

Abedini A, Calagari AA (2015) Geochemical characteristics of the Abgarm kaolin deposit, NW Iran. Neues Jahrbuch Fur Geologie Und Palaontologie - Abhandlungen 278(3):335–350. https://doi.org/10.1127/njgpa/2015/0533

Argus DF, Gordon RG, Demets C, Stein S (1989) Closure of the Africa-Eurasia-North America Plate motion circuit and tectonics of the Gloria Fault. J Geophys Res 94(B5):5585–5602. https://doi.org/10.1029/JB094iB05p05585

Armstrong-Altrin JS, Verma SP, Madhavaraju J, Lee YIl, Ramasamy S (2003) Geochemistry of upper Miocene Kudankulam limestones, Southern India. Intl Geol Rev 45(1):16–26https://doi.org/10.2747/0020-6814.45.1.16

Baiyegunhi C, Liu K, Gwavava O (2017) Diagenesis and reservoir properties of the Permian Ecca Group sandstones and mudrocks in the Eastern Cape Province.South Africa. Minerals7(6):doi:https://doi.org/10.3390/min7060088

Bakkiaraj D, Nagendra R, Nagarajan R, Armstrong-Altrin JS (2010) Geochemistry of sandstones from the Upper Cretaceous Sillakkudi Formation, Cauvery Basin, southern India: implication for provenance. J Geol Soc India 76(5):453–467

Bau M, Dulski P (1996) Distribution of yttrium and rare-earth elements in the Penge and Kuruman iron-formations, Transvaal Supergroup South Africa. Precambrian Research 79(1–2):37–55

Beach A, Tarne J (1978) Major and trace element patterns established during retrogressive metamorphism of granulite-facies gneisses NW Scotland. Precambrian Res 7(4):325–348

Bejaoui J, Bouhlel S, Barca D, Braham A (2011) Le champ filonien à Zn-(Pb, Cu, As, Hg) du district minier de Fedj Hassène (Nord Ouest de la Tunisie): Minéralogie, Eléments en traces, Isotopes du Soufre et Inclusions Fluides. Estudios Geologicos 67(1):5–20. https://doi.org/10.3989/egeol.40214.118

Bekker A, Slack JF, Planavsky N, Krapez B, Hofmann A, Konhauser KO, Rouxel OJ (2010) Iron formation: the sedimentary product of a complex interplay among mantle, tectonic, oceanic, and biospheric processes. Econ Geol 105(3):467–508

Bhatia MR, Crook KAW (1986) Trace element characteristics of graywackes and tectonic setting discrimination of sedimentary basins. Contrib Miner Petrol 92(2):181–193. https://doi.org/10.1007/BF00375292

Bilenker LD, Simon AC, Reich M, Lundstrom CC, Gajos N, Bindeman I, Barra F, Munizaga R (2016) Fe–O stable isotope pairs elucidate a high-temperature origin of Chilean iron oxide-apatite deposits. Geochim Cosmochim Acta 177:94–104

Bouedja F (2010) Tectonique actuelle et récente et risque sismique de la région de Constantine. Diseertation, University of Ferhat Abbas-Setif

Bouillin JP (1986) Le" bassin maghrebin" une ancienne limite entre l'Europe et l'Afrique a l'ouest des Alpes. Bulletin De La Société Géologique De France 2(4):547–558

Bouzenoune A, Lécolle P (1997) Petrographic and geochemical arguments for hydrothermal formation of the Ouenza siderite deposit (NE Algeria). Miner Deposita 32(2):189–196

Caire A (1957) Étude géologique de la région des Bibans (Algérie). Dissertation, University of Toulouse

Chabbi A (2017) Les nappes telliennes de la région Nord de Souk Ahras (NE algérien) : Etude géologique et structurale. Dissertation, University of Badji Mokhtar-Annaba

Chadi M (1991) Géologie des monts d'Ain m'lila (Algérie orientale). Dissertation, University of Henri Poincaré-Nancy 1

Chazot G, Abbassene F, Maury RC, Déverchère J, Bellon H, Ouabadi A, Bosch D (2017) An overview on the origin of post-collisional Miocene magmatism in the Kabylies (northern Algeria): evidence for crustal stacking, delamination and slab detachment. J Afr Earth Sc 125:27–41. https://doi.org/10.1016/j.jafrearsci.2016.10.005

Childress TM, Simon AC, Day WC, Lundstrom CC, Bindeman IN (2016) Iron and oxygen isotope signatures of the pea ridge and

pilot knob magnetite-apatite deposits, Southeast Missouri, USA. Econ Geol 111(8):2033–2044. https://doi.org/10.2113/econgeo.111.8.2033

Ciccioli PL, Limarino CO, Isabbell JL, Taboada AC, Pagani MA, Gulbranson EL (2020) Interpreting detrital modes and geochemistry of sandstones from the late Paleozoic Tepuel-Genoa Basin: Paleogeographic implications (Patagonia, Argentina). J S Am Earth Sci 104:1–52

Clayton RN, Epstein S (1961) The use of oxygen isotopes in high-temperature geological thermometry. J Geol 69(4):447–452

Cole DR, Horita J, PolyakovVB VJW, Spicuzza MJ, Coffey DW (2004) An experimental and theoretical determination of oxygen isotope fractionation in the system magnetite-H2O from 300 to 800 °C. Geochim Cosmochim Acta 68(17):3569–3585. https://doi.org/10.1016/j.gca.2004.02.017

Cox R, Lowe DR, Cullers RL (1995) The influence of sediment recycling and basement composition on evolution of mudrock chemistry in the southwestern United States. Geochim Cosmochim Acta 59(14):2919–2940. https://doi.org/10.1016/0016-7037(95)00185-9

David L (1956) Etude géologique de la haute Medjerda. In: Bulletin Service de la carte géologique de l'Algérie

De Baar HJW, Bacon MP, Brewer PG, Bruland KW (1985) Rare earth elements in the Pacific and Atlantic Oceans. Geochim Cosmochim Acta 49(9):1943–1959. https://doi.org/10.1016/0016-7037(85)90089-4

De Baar HJW, German CR, Elderfield H, Van Gaans P (1988) Rare earth element distributions in anoxic waters of the Cariaco Trench. Geochim Cosmochim Acta 52(5):1203–1219

Derry LA, Jacobsen SB (1990) The chemical evolution of Precambrian seawater: evidence from REEs in banded iron formations. Geochim Cosmochim Acta 54(11):2965–2977. https://doi.org/10.1016/0016-7037(90)90114-Z

Dill HG, Weber B, Kaufhold S (2009) The origin of siderite-goethite-phosphate mineralization in the karst-related faultbound iron ore deposit Auerbach, Germany, a clue to the timing of hypogene and supergene Fe-Al phosphates in NE Bavaria. Neues Jahrb Mineral Abh 186(3):283–307. https://doi.org/10.1127/0077-7757/2009/0149

Dobbins MS, Burnet G (1982) Production of an iron ore concentrate from the iron-rich fraction of power plant fly ash. Resour Conserv 9:231–242

Dreesen R (1989) Oolitic ironstones as event-stratigraphical marker beds within the Upper Devonian of the Ardenno-Rhenish Massif. Geol Soc Spec Pub 46(46):65–78. https://doi.org/10.1144/GSL.SP.1989.046.01.08

Dubourdieu GG (1957) Étude géologique de la région de l'Ouenza:(confins algéro-tunisiens). Dissertation, Université of Paris

Einsele G Ricken W, Seilacher A (1991) Cycles and events in stratigraphy

El Hefnawi MA, Mashaly AO, Shalaby BN, Rashwan MA (2010) Petrography and geochemistry of eocene limestone from Khashm Al-Raqaba area, El-Galala El-qibliya Egypt. Carbonates and Evaporites 25(3):193–202. https://doi.org/10.1007/s13146-010-0023-4

Elderfield H, Greaves MJ (1982) The rare earth elements in seawater. Nature 296(5854):214–219

Fatiou AKI, Konaté M, Yessoufou S, Glodji CLA, Heckmann M, Saley HG (2019) Geology, mineralogy and geochemistry of the oligocene oolitic iron ore of the Continental Terminal Formation, Kandi Basin North East Benin. Intl J Geosci 10(04):491–512. https://doi.org/10.4236/ijg.2019.104029

Feng R, Kerrich R (1990) Geochemistry of fine-grained clastic sediments in the Archean Abitibi greenstone belt, Canada: implications for provenance and tectonic setting. Geochim Cosmochim Acta 54(4):1061–1081. https://doi.org/10.1016/0016-7037(90)90439-R

Ferhi F, Kadri A, Chihi L, Houla Y (2018) Le rôle des failles E-W dans la structuration du jebel Rhoualguia et des secteurs avoisinants (région de Thala-Rohia, Tunisie centrale) Gravity analysis and interpretation View project Rôle des décrochements E-W dans l'évolution géodynamique de NW de la T. January. https://www.researchgate.net/publication/326017058

Figari EG, Scasso RA, Cúneo RN, Escapa I (2015) Estratigrafía y evolución geológica de la cuenca de Cañadón Asfalto, Provincia del Chubut, Argentina. Latin Am J Sediment Basin Anal 22(2):135–169

Garnit H, Bouhlel S (2017) Petrography, mineralogy and geochemistry of the Late Eocene oolitic ironstones of the Jebel Ank, Southern Tunisian Atlas. Ore Geol Rev 84:134–153. https://doi.org/10.1016/j.oregeorev.2016.12.026

Gràcia E, Danobeitia J, Vergés J, Bartolomé R, Córdoba D (2003) Crustal architecture and tectonic evolution of the Gulf of Cadiz (SW Iberian margin) at the convergence of the Eurasian and African plates. Tectonics22(4). doi:https://doi.org/10.1029/2001tc901045

Halimi F (2008) Etude géologique et géostatistique du gisement de Fer de Châabet El Ballout –Souk Ahras- (N-E algérien). Dessertation,University of Badji Mokhtar-Annaba

Herron MM (1988) Geochemical classification of terrigenous sands and shales from core or log data. J Sediment Res 58(5):820–829

Hlaiem A (1999) Halokinesis and structural evolution of the major features in eastern and southern Tunisian Atlas. Tectonophysics 306(1):79–95. https://doi.org/10.1016/S0040-1951(99)00045-1

Johnson CM, Beard BL, Klein C, Beukes NJ, Roden EE (2008) Iron isotopes constrain biologic and abiologic processes in banded iron formation genesis. Geochim Cosmochim Acta 72(1):151–169. https://doi.org/10.1016/j.gca.2007.10.013

Johnson JE, Web SM, Thomas K, OnoS KJL, Fischer WW (2013) Manganese-oxidizing photosynthesis before the rise of cyanobacteria. Proc Natl Acad Sci USA 110(28):11238–11243. https://doi.org/10.1073/pnas.1305530110

Kennedy MJ, RunnegarB PAR, Hoffmann KH, Arthur MA (1998) Two or four Neoproterozoic glaciations? Geology 26(12):1059–1063. https://doi.org/10.1130/0091-7613(1998)026%3c1059:TOFNG%3e2.3.CO;2

Klein C, Beukes NJ (1993) Sedimentology and geochemistry of the glaciogenic late Proterozoic Rapitan iron-formation in Canada. Econ Geol 88(3):542–565

Knipping JL, Bilenker LD, Simon AC, Reich M, Barra F, Deditius AP, Wälle M, Heinrich CA, Holtz F, Munizaga R (2015) Trace elements in magnetite from massive iron oxide-apatite deposits indicate a combined formation by igneous and magmatic-hydrothermal processes. Geochim Cosmochim Acta 17:15–38

Koteswara RD, Raju GVRP, Sowjanya C, Rao JP (2011) Laboratory studies on the properties of stabilized marine clay from Kakinada Sea Coast, India. International Journal of Engineering Science and Technology (IJEST)3(1):421–428

Kouzmine G (1992) Gisement de Fer de Chaabet EL Bellout .In: interneal rapport of Somifer

Kraiem Z, Zouari K, Bencheikh N, Agoun A, Abidi B (2015) Processus de minéralisation de la nappe du Plio-Quaternaire dans la plaine de Segui-Zograta (Sud-Ouest tunisien). Hydrol Sci J 60(3):534–548. https://doi.org/10.1080/02626667.2013.877587

Kriviakine B, Kovalenko E, Vnouchkov V (1989) Carte géologique de Souk Ahras

Madre M (1969) Contribution à l'étude géologique et métallogénique du Djebel Ouenza (Est Algérien).Dessertation,University of Paris

Mahjoubi H, Samama J (1983) Modele de concentrationsupergéne d'amas sidéritique: le cas du Jebel Jérissa, Tunisie. Bull. Soc. Géol. Fr, 91–99

Martinez C, Chikhaoui M, Truillet R, Ouali J, Creuzot G (1991) Le contexte géodynamique de la distension albo-aptienne en Tunisie septentrionale et centrale : structuration éocrétacée de l'Atlas tunisien. Eclogae Geologicae Helveticae 84(1):61–82

Marzougui W, Melki F, Arfaoui M, Houla Y, Zargouni F (2015) Major faults, salt structures and paleo-ridge at tectonic nodes in Northern Tunisia: contribution of tectonics and gravity analysis. Arab J Geosci 8(9):7601–7617. https://doi.org/10.1007/s12517-014-1698-y

McLennan SM, McCulloch MT, Taylor SR, Maynard JB (1989) Effects of sedimentary sorting on neodymium isotopes in deep-sea turbidites. In Nature (Vol. 337, Issue 6207):547–549. doi:https://doi.org/10.1038/337547a0

Mehdipour Ghazi, J, Harris C, Rahgoshay M, Moazzen M (2019) Combined igneous and hydrothermal source for the Kiruna-type Bafq magnetite-apatite deposit in Central Iran; trace element and oxygen isotope studies of magnetite. Ore Geology Reviews105(May 2018):590–604 doi:https://doi.org/10.1016/j.oregeorev.2019.01.006

Michard A, Michard G, Stüben D, Stoffers P, Cheminée JL, Binard N (1993) Submarine thermal springs associated with young volcanoes: the Teahitia vents, Society Islands Pacific Ocean. Geochimica Et Cosmochimica Acta 57(21–22):4977–4986. https://doi.org/10.1016/S0016-7037(05)80003-1

Nath BN, Bau M, Rao BR, Rao CM (1997) Trace and rare earth elemental variation in Arabian Sea sediments through a transect across the oxygen minimum zone. Geochim Cosmochim Acta 61(12):2375–2388

Nesbitt HW, Fedo CM, Young GM (1997) Quartz and feldspar stability, steady and non-steady-state weathering, and petrogenesis of siliciclastic sands and muds. J Geol 105(2):173–191. https://doi.org/10.1086/515908

Nyström JO, Billström K, Henríquez F, Fallick AE, Naslund HR (2008) Oxygen isotope composition of magnetite in iron ores of the Kiruna type in Chile and Sweden. GFF 130(4):177–188. https://doi.org/10.1080/11035890809452771

Otake T, Wesolowski DJ, Anovitz LM, Allard LF, Ohmoto H (2007) Experimental evidence for non-redox transformations between magnetite and hematite under H2-rich hydrothermal conditions. Earth Planet Sci Lett 257(1–2):60–70. https://doi.org/10.1016/j.epsl.2007.02.022

Perthuisot V, Guilhaumou N, Touray JC (1978) Les inclusions fluides hypersalines et gazeuses des quartz et dolomites du Trias evaporitique Nord-tunisien; essai d'interpretation geodynamique. Bulletin de La Société Géologique de France, S7-XX(2): 145–155. doi:https://doi.org/10.2113/gssgfbull.s7-xx.2.145

Perthuisot V (1978) Dynamique et pétrogenèse des extrusions triasiques de Tunisie septentrionale. Dissertation, École Normale Supérieure, Lyon

Perthuisot V, Bouzenoune A, Hatira N, Henry B, Laatar E, Mansouri A, Rouvier H, Smati A, Thibieroz J (1999) Les diapirs du Maghreb oriental; part des deformations alpines et des structures initials cretacees et eocenes dans les formes actuelles. Bulletin De La Société Géologique De France 170(1):57–65

Pohl W, AmouriM KO, Scheffer R, Zachmann D (1986) A new genetic model for the North African metasomatic siderite deposits. Miner Deposita 21(3):228–233. https://doi.org/10.1007/BF00199805

Pourmand A, Dauphas N, IrelandTJ (2012) A novel extraction chromatography and MC-ICP-MS technique for rapid analysis of REE, Sc and Y: revising CI-chondrite and Post-Archean Australian Shale (PAAS) abundances. Chem Geol 291:38-54https://doi.org/10.1016/j.chemgeo.2011.08.011

Raoult JF and JF R (1974) Geologie du centre de la chaine numidique (nord du Constantinois, Algerie)

Rhodes AL, Oreskes N (1999) Oxygen isotope composition of magnetite deposits at El. Laco, Chile evidence of formation from isotopically heavy fluids

Rudis (1964) Association industrielle et minière, Trbovlje Service géologique - Ljubljana: Recherche geologiques a chabet ballout effectuées en 1963/64.In: Bulletin Service géologique de l'Algérie

Said A (2011) Tectonique active de l'Atlas Sud Tunisien: approche structurale et morphotectonique.Dissertation, University of Toulouse III

Talbi F, Melki F, Ismail-Lattrache K, Ben-Alouani R, Tlig S (2008) Le Numidien de la Tunisie septentrionale: Données stratigraphiques et interprétation géodynamique. Estudios Geologicos 64(1):31–44. https://doi.org/10.3989/egeol.08641429

Taylor HP, Frechen J, Degens ET (1967) Oxygen and carbon isotope studies of carbonatites from the Laacher See District, West Germany and the Alnö District Sweden. Geochimica Et Cosmochimica Acta 31(3):407–430. https://doi.org/10.1016/0016-7037(67)90051-8

Temur S, Orhan H, Deli A (2009) Geochemistry of the limestone of Mortas Formation and related terra rossa, Seydisehir, Konya Turkey. Geochem Intl 47(1):67–93. https://doi.org/10.1134/S0016702909010054

Thibiéroz J, Madre M (1976) Le gisement de sidérite du Djebel Ouenza (Algérie) est controlé par par un golfe de la mer aptienne.Bull Soc Hist Nat Afrique Nord/Alger 67:125–149

Thomsen KJ, Murray AS, Jain M, Bøtter-Jensen L (2008) Laboratory fading rates of various luminescence signals from feldspar-rich sediment extracts. Radiat Meas 43(9–10):1474–1486

Thorne W, Hagemann S, Vennemann T, Oliver N (2009) Oxygen isotope compositions of iron oxides from high-grade BIF-hosted iron ore deposits of the central Hamersley province, Western Australia: constraints on the evolution of hydrothermal fluids. Econ Geol 104(7):1019–1035. https://doi.org/10.2113/gsecongeo.104.7.1019

Vila JM (1980) La chaîne alpine d'Algérie orientale et des confins algérotunisiens.Thèse Doct ès Science Naturelle. Université Pierre et Marie Curie, France. 665 p

Weis F, Troll VR (2013) Oxygen and iron isotope systematics of the Grängesberg Mining District (GMD), Central Sweden. Examensarbete Vid Institutionen För Geovetenskaper, 251(251): 82. http://urn.kb.se/resolve?urn = urn:nbn:se:uu:diva-192216

Winchester JA, Floyd PA (1977) Geochemical discrimination of different magma series and their differentiation products using immobile elements. Chemical Geology, 20(C):325–343. doi:https://doi.org/10.1016/0009-2541(77)90057-2

Wronkiewicz DJ, Condie KC (1987) Geochemistry of Archean shales from the Witwatersrand Supergroup, South Africa: source-area weathering and provenance. Geochim Cosmochim Acta 51(9):2401–2416. https://doi.org/10.1016/0016-7037(87)90293-6

Yang XQ, Zhang ZH, Duan SG, Zhao XM (2015) Petrological and geochemical features of the Jingtieshan banded iron formation (BIF): a unique type of BIF from the Northern Qilian Orogenic Belt, NW China. J Asian Earth Sci 113:1218–1234. https://doi.org/10.1016/j.jseaes.2015.03.024

Zanouda HS, Laouar R, Salmi-Laouar S, Sebai A, Verati, C, Bouhlel S, Boyce AJ (2019) The Sidi El Hemissi Triassic "ophites" (Souk Ahras, NE Algeria): petrology, geochemistry, and petrogenesis. Arabian Journal of Geosciences12(8) doi:https://doi.org/10.1007/s12517-019-4462-5

Zouaghi T, Bédir M, Hédi Inoubli M (2005) The Albian-Maastrichtian deep structuring in central Tunisia: a new limit of the Kasserine Islets and geodynamic implications. Comptes Rendus - Geoscience 337(7):685–693. https://doi.org/10.1016/j.crte.2005.02.006